Aggravated surface O_3 pollution primarily driven by meteorological variation in China during the ~~e~~2020~~arly~~ COVID-19 pandemic lockdown period

Zhendong Lu[1*], Jun Wang[1,2*], Yi Wang[2,3], Daven K. Henze[4], Xi Chen[2], Tong Sha[2,5], Kang Sun[6,7]

[1]*Interdisciplinary Graduate Program in Informatics, The University of Iowa, Iowa City, IA, United States*

[2]*Department of Chemical and Biochemical Engineering, Center for Global and Regional Environmental Research and Iowa Technology Institute, The University of Iowa, Iowa City, IA, United States*

[3]*Now at Hubei Key Laboratory of Regional Ecology and Environmental Change, School of Geography and Information Engineering, China University of Geosciences, Wuhan, China*

[4]*Department of Mechanical Engineering, University of Colorado, Boulder, CO, United States*

[5]*Now at ~~Collaborative Innovation Center on Forecast and Evaluation of Meteorological Disasters (CIC-FEMD), Key Laboratory for Aerosol-Cloud-Precipitation of China Meteorological Administration, Nanjing University of Information Science and Technology, Nanjing, China~~School of Environmental Science and Engineering, Shaanxi University of Science and Technology, Xi'an, China*

[6]*Department of Civil, Structural and Environmental Engineering, University at Buffalo, Buffalo, NY, United States*

[7]*Research and Education in Energy, Environment and Water Institute, University at Buffalo, Buffalo, NY, United States*

*Correspondence to: Jun Wang (jun-wang-1@uiowa.edu) and Zhendong Lu (zhendong-lu@uiowa.edu)

Submitted: November 2023

Revised: April 2024

Abstract

Due to the lockdown during the COVID-19 pandemic in China from late January to early April in 2020, a significant reduction of primary air pollutants, as compared to the same time period in 2019, has been identified by satellite and ground observations. However, this reduction is in contrast with the increase of surface O_3 concentration in many parts of China during the same period from 2019 to 2020. The reasons for this contrast are studied here from two perspectives: emission changes and inter-annual meteorological variations. Based on top-down constraints of NOx emissions from TROPOMI measurements and GEOS-Chem model simulations, our analysis reveals that NOx and volatile organic compound (VOC) emission reductions as well as meteorological variations lead to 8%, -3%, and 1% changes in O_3 over North China, respectively. In South China, however, we find that meteorological variations cause ~30% increases in O_3, which is much larger than -1% and 2% changes due to VOC and NOx emission reductions, respectively, and the overall O_3 increase in the simulations is consistent with the surface observations. The higher temperature associated with increase of solar radiation and declined relative humidity are~~is~~ the main reasons that lead~~s~~ to the surface O_3 increase in South China. ~~Overall~~Collectively, inter-annual meteorological variations have a larger impact than emission reductions on the aggravated surface O_3 pollution in China during the ~~early~~ lockdown period of COVID-19 pandemic.

1. Introduction

Surface ozone (O_3), an important air pollutant that is harmful to human health (Jerrett et al., 2009) and stomatal conductance of green vegetations (Gong et al., 2020), is produced by photochemical reactions of nitrogen oxides (NOx) and volatile organic compounds (VOC) (Liu et al., 1987; Sillman et al., 1990). In addition to emissions, meteorological conditions, such as temperature, solar radiation and relative humidity, also have large impacts on surface O_3 formation (Lu et al., 2019).

Ground observations show that surface O_3 increased dramatically during the COVID-19 lockdown period in China by around 40% on average (Tong et al., 2023) and even larger than 100% (Shi and Brasseur, 2020; Liu et al., 2021) depending on the time period and region. The reduction of economic activities during the lockdown period led to a significant decrease of several primary air pollutants emissions. The NO_2 vertical column density (VCD) from satellite measurements and

surface NO_2 concentration from ground measurements were reduced by 40% - 60% in China during the lockdown period (Bauwens et al., 2020; Shi and Brasseur, 2020; Liu et al., 2020a; Zhang et al., 2020). A lower but discernible reduction of sulfur dioxide (SO_2), carbon monoxide (CO), and formaldehyde (HCHO) have also been identified by satellite or ground-based observations in China (Shi and Brasseur, 2020; Levelt et al., 2022; Ghahremanloo et al., 2021). However, during this period surface O_3 concentrations increased, and the respective roles of meteorological factor and emission reduction for the aggravated surface O_3 pollution during the lockdown in China need to be further quantified.

This study provides a quantitative analysis of the causes for the unexpectedly aggravated surface O_3 pollution in China during the ~~early~~ lockdown period of the pandemic from two perspectives using GEOS-Chem model. One is anthropogenic emission reduction of NOx and VOC in response to the lockdown possibly under a VOC-limiting chemical regime of surface O_3 production (Guo et al., 2023), while the other is the impact of natural variability of meteorological conditions. Previous studies have reported the enhanced surface O_3 due to NOx emission decline during the lockdown period in North China using chemical transport model (CTM) simulations without controlling for the impacts of meteorological variability (Zhang et al., 2021; Huang et al., 2020; Miyazaki et al., 2020). Other studies quantified or excluded the meteorological impacts on the surface O_3 using statistical analysis instead of CTM that account for the physical and chemical processes (Venter et al., 2020; Bi et al., 2022; Tong et al., 2023). Although a few studies have investigated the contributions from both emission reduction and meteorological variability to surface O_3 increase using CTMs, most of their results have uncertainties due to the limitations of their analysis. For example, some of them keep the emissions unchanged (Zhao et al., 2020) or assume an arbitrarily uniform emission reduction instead of constraining the emission based on observations (Le et al., 2020; Liu et al., 2021). In cases where the emissions were constrained by the observations, the focus was limited to several cities in China (Liu et al., 2020b). Furthermore, in the past studies, the surface O_3 increase during the lockdown period of 2-4 weeks is quantified in reference to the time period right before the lockdown instead of the same period in previous years; such comparisons by design cannot exclude the possibility that the seasonal variation of meteorology from early January to early April may have dominated the cause for the surface O_3 increase. A comprehensive analysis of the contributions from emission reductions and

meteorological variations to the surface O_3 increase during the first round of the lockdown period with respect to the same time period in previous years in China is therefore overdue.

Here, we apply a top-down method to update NOx and VOC emission in February and March in 2020 based on the TROPOMI NO_2 and formaldehyde (HCHO) product. A set of GEOS-Chem model simulations with NOx and VOC emissions and meteorological fields in different time periods are then conducted. Based on the difference in surface O_3 concentration in different modeling sensitivity experiments, we quantitatively assess the respective roles of emission and meteorology in regulating surface O_3 concentration in continental China. The ground observations of surface O_3 and NO_2 concentration are compared with the model simulations to verify our analysis. Section 2 introduces the satellite and ground-based measurements, NOx emission update scheme, and the configurations of GEOS-Chem simulation experiments. Section 3 provides an evaluation of the constrained NOx emission and surface O_3 simulations. The analysis of the mechanism of the aggravated surface O_3 pollution is presented in Section 4, followed by the summary and conclusions in Section 5.

2. Datasets and Methods

2.1 TROPOMI NO_2 and HCHO product

We used tropospheric NO_2 and HCHO level 2 VCD product provided by the Tropospheric Monitoring Instrument (TROPOMI) onboard the Sentinel-5 Precursor (S5P) satellite (Veefkind et al., 2012). S5P is a sun-synchronous polar orbit satellite launched on 13 October 2017, which covers the near-global domain in a single day. TROPOMI provides NO_2 and HCHO retrievals at an approximately 7 km x 3.5 km spatial resolution (5.5km x 3.5 km since 6 August 2019) from the ascending orbit with an equatorial crossing time of ~13:30 local time (Van Geffen et al., 2020; De Smedt et al., 2018). The datasets were obtained from the NASA Goddard Earth Sciences Data and Information Services Center (https://daac.gsfc.nasa.gov). A quality control procedure similar to Bauwens et al. (2020) but with slightly stricter criteria is adopted for TROPOMI NO_2 and HCHO data. The TROPOMI retrievals under one or more than one of the following conditions are screened out for data quality control. (1) Quality assurance value is no larger than 0.5; (2) cloud radiance fraction within NO_2 or HCHO retrieval window is larger than 0.3; (3) solar zenith angle is larger than 70°; and (4) viewing zenith angle is larger than 70°.

2.2 Ground O_3 and NO_2 measurements

Surface measurements of O_3 and NO_2 were collected from ~1600 operational air quality monitoring stations over the mainland China managed by the China National Environmental Monitoring Center (http://www.cnemc.cn/en/). We calculated daily maximum 8-hour average (MDA8) O_3 concentration from hourly in situ measurements. Surface O_3 are measured by ultraviolet photometric method and Indigo disulfonate spectrophotometry, following the national environmental standards of HJ 590-2010 and HJ 504-2009. Surface NO_2 concentrations are measured by the chemiluminescence method (Zhang and Cao, 2015) that quantifies the NO_2 concentrations by measuring the NO decomposed from NO_2, which can cause a positive bias in the NO_2 measurements (Steinbacher et al., 2007) because NOz (compounds produced from the atmospheric oxidation of NOx) can also be decomposed to NO. The true NO_2 concentrations only account for 43%-76% and 70%-83% of measured values for rural and urban sites (Steinbacher et al., 2007). Following Wang et al. (2020b), we also applied a correction factor but with a lower value of 0.75 to the measured NO_2, considering that we included both rural and urban sites. The sampling ports are placed at 3 to 15 meters above the ground following the national environmental monitoring method standard HJ 664-2013. The measured data are reported in the unit of $\mu g\ m^{-3}$ under standard temperature (273.15 K) and pressure (101.325 kPa) according to national environmental standards GB 3095-2012.

2.3 GEOS-Chem model and its adjoint

The global 3-D chemical transport model GEOS-Chem (Bey et al., 2001) version 12.7.2 is used here. We apply the nested-grid version of GEOS-Chem (Chen et al., 2009; Wang et al., 2004) with the horizontal resolution of 0.25°×0.3125° and 47 vertical hybrid-sigma levels over East Asia (70°E-140°E, 15°N-55°N). The boundary conditions are obtained from the 2°×2.5° global simulation. The model is driven by the GEOS-FP meteorological field provided by NASA Global Modeling and Assimilation Office (GMAO). A detailed O_3-NOx-hydrocarbon chemistry (Mao et al., 2010; Mao et al., 2013; Travis et al., 2016) is included in the GEOS-Chem model. The altitude of the surface O_3 output from GEOS-Chem is specified at 9 meters above the ground to match the in-situ measurements (Travis et al., 2017; Zhang et al., 2012). Through our sensitivity test using GEOS-Chem, the variation of surface O_3 from 3 to 9 meters above the surface is generally less than 0.723 ppb (75th percentile), and the median bias is 0.283 ppb. Travis et al. (2017) reported

from 60 m to 10 m above the ground, the MDA8 O_3 could decrease by ~3 ppb. Therefore, when comparing GEOS-Chem surface O3 with in-situ measurements, the differences caused by inconsistent reported altitudes (9 m versus 3-15 m) can be ignored.

The global anthropogenic emission used in GEOS-Chem model is the Community Emissions Data System (CEDS) inventory (Hoesly et al., 2018), which is replaced by the MIX inventory (Li et al., 2017) over the Asian region. Biogenic emissions for VOCs follows the Model of Emissions of Gases and Aerosols from Nature (MEGAN) inventory (Guenther et al., 2012). Natural NOx emissions includes biomass burning from GFED4 inventory (Van Der Werf et al., 2017), soil NOx emissions (Hudman et al., 2012) and lightning sources (Murray et al., 2012; Ott et al., 2010).

The adjoint of the GEOS-Chem model (Henze et al., 2007; Henze et al., 2009) is a component of the 4D-Var inversion method that can efficiently optimize spatially disaggregated aerosol and gas emissions. This is done through iterative minimization of a cost function using the model adjoint to calculate the gradient of the cost function with respect to a large number of model parameters (such as anthropogenic NOx emissions in each grid box) simultaneously. The cost function is the sum of the error weighted difference between forward model outputs and observations and the divergence of posterior model parameters from the prior estimate (Section 2.4). We developed and validated the observation operator for TROPOMI NO_2 in the GEOS-Chem adjoint model version 35n similar to Wang et al. (2020a) and used it to optimize the anthropogenic NOx emission during the lockdown period in China. The monthly NOx emission optimization is implemented using the 4D-Var method with GEOS-Chem adjoint at the nested grid with the resolution of 0.25°×0.3125° via assimilating the daily TROPOMI NO_2 measurements. The prior anthropogenic NOx emission used in the GEOS-Chem adjoint is HTAP version 2 (Janssens-Maenhout et al., 2015), which is equivalent to the MIX inventory in East Asia (Li et al., 2017).

2.4 NOx and VOC emission updates

Two approaches are used to update the emissions during the lockdown period in 2020. The first is a simple mass balance approach (Leue et al., 2001; Martin et al., 2003; Vinken et al., 2014) for updating the NOx emission by assuming a constant NOx lifetime and NOx/NO_2 ratio. In the period from 2010 to 2019, the anthropogenic NOx emissions have declined significantly as a result of the clean air actions of Chinese government (Zheng et al., 2018). We scale the anthropogenic

NOx emission from year 2010 to 2019 using the spatially gridded ratio of mean TROPOMI tropospheric NO_2 VCD in Feb.-Mar. 2019 to GEOS-Chem simulated NO_2 column with default MIX 2010 emission (Appendix A), to obtain the baseline anthropogenic NOx emission in 2019, which is denoted as MIX 2019. To derive anthropogenic NOx emissions in 2020 in China during the COVID-19 lockdown (MIX 2020), the spatially gridded ratio of mean TROPOMI tropospheric NO_2 VCD in 2020 Feb.-Mar. to that in 2019 Feb.-Mar. is taken as a scaling factor for the updated baseline anthropogenic NOx emission in 2019 (MIX 2019). The two-month mean of TROPOMI NO_2 VCD in 2019 and 2020 are calculated with the physical oversampling procedure (Sun et al., 2018). Scaling factors in regions where mean TROPOMI tropospheric NO_2 VCD in 2019 Feb.-Mar. is less than 0.1 Dobson unit (DU) are set to 1 for emission updates in both 2020 and 2019, assuming that the lockdown only affects the populated areas (that have high NO_2 in 2019).

The second method for updating NOx emission is 4D-Var via the GEOS-Chem adjoint model. The anthropogenic NOx emissions in 2020 lockdown period derived from the GEOS-Chem adjoint is denoted as 2020 Adjoint. Following Wang et al. (2020a), the cost function J for optimizing the NOx emission is defined as

$$J = \frac{1}{2}\sum_{\boldsymbol{c}\in\Omega}[H(\boldsymbol{c}) - \boldsymbol{s}]^{\mathrm{T}}\boldsymbol{S}_{\mathrm{obs}}^{-1}[H(\boldsymbol{c}) - \boldsymbol{s}] + \frac{1}{2}\gamma(\boldsymbol{\sigma} - \boldsymbol{\sigma}_a)^{\mathrm{T}}\boldsymbol{S}_a^{-1}(\boldsymbol{\sigma} - \boldsymbol{\sigma}_a) \quad (1)$$

where $\boldsymbol{s}$ is the tropospheric slant column density of TROPOMI NO_2, which is the product of TROPOMI NO_2 VCD and air mass factor. H is the TROPOMI NO_2 observation operator that maps the modeled NO_2 concentrations $\boldsymbol{c}$ to the observations in time and space and calculates the corresponding slant column density to make an apple-to-apple comparison of the model to TROPOMI. Ω is the spatial and temporal domain where both model simulations and observations are available. $\boldsymbol{\sigma}$ is the scaling factor of anthropogenic NOx emissions to be optimized, and $\boldsymbol{\sigma}_a$ is the prior emission scaling factors, which equals 1. $\boldsymbol{S}_{\mathrm{obs}}$ and $\boldsymbol{S}_a$ are observational and prior error covariance matrices, respectively. γ is the regularization factor that balances the weights of the observational term and prior term. We assumed $\boldsymbol{S}_{\mathrm{obs}}$ to be diagonal following Wang et al. (2020a) with the diagonal values calculated as the square of the standard error of tropospheric NO_2 slant column density from the TROPOMI product. The prior error of the NOx emissions is assumed to be 100%. The spatial correlation of NOx emissions is considered in this study, and the off-diagonal elements of $\boldsymbol{S}_a$ are computed by assuming an exponentially decaying error correlation with a fixed

decaying distance of 150 km following Qu et al. (2017). The γ value was determined as 500 via the total error minimization and L-curve test (Henze et al., 2009; Qu et al., 2017).

We developed the observation operator for TROPOMI NO_2 product in the GEOS-Chem adjoint model with GEOS-Chem NO_2 vertical profiles and TROPOMI NO_2 averaging kernel applied to minimize the discrepancies between the assumptions in TROPOMI NO_2 retrieval and GEOS-Chem model simulation. See Appendix B for additional details. The observation operator has been validated using the finite difference method (Appendix C).

For anthropogenic VOC emissions update, we only applied the mass balance method based on the TROPOMI HCHO data. The default anthropogenic VOC emissions used in the GEOS-Chem is also MIX 2010 (Li et al., 2017). We ignore the change of anthropogenic VOC emissions from 2010 to 2019 (Appendix D). The baseline VOC emission in 2019 (MIX 2019) is identical to that of MIX 2010. The updated anthropogenic VOC emissions during the lockdown period is denoted as MIX 2020. HCHO is one species of VOC and may not be able to represent other VOC species. Different from NOx, biogenic sources, meteorological impacts, and large retrieval uncertainty of HCHO due to its low optical depth prevent accurately quantifying the emission decline due to lockdown from satellite retrievals (Levelt et al., 2022). Vigouroux et al. (2020) reported that TROPOMI HCHO tends to be overestimated by ~26% for HCHO column lower than 2.5×10^{15} molecules cm^{-2} and underestimated by ~31% for HCHO column higher than 8.0×10^{15} molecules cm^{-2}. To optimize the signal, we spatially aggregate the ratio of TROPOMI HCHO in 2020 Feb.-Mar.~~during the lockdown period~~ to that in 2019 Feb.-Mar.~~before the lockdown~~ to the resolution of 0.5°, which are used as the scaling factors for updating the anthropogenic VOC emissions during the lockdown period. The aggregation is based on the oversampling of TROPOMI HCHO at 0.01° resolution, and the ratio is computed as the mean of the lowest 25th percentile of all ratios at 0.01° resolution in each 0.5°×0.5° grid box, which ensures that only statistically significant changes are considered. We assumed the change of anthropogenic VOC emissions over sparsely populated areas (TROPOMI NO_2 in 2019 Feb.-Mar. less than 0.1 DU) is insignificant and assigned the ratio values as one. To further evaluate the uncertainties associated with this approach, we also conducted sensitivity study by using different threshold in the aggregation.

We assess the results from model experiments (as described in Section 2.5) adopting the updated NOx emission by comparing mean tropospheric NO_2 VCD from GEOS-Chem and from

TROPOMI observations in Feb.-Mar. of 2019 and 2020. The averaging kernel of TROPOMI NO_2 is applied to modeled NO_2 column for this comparison, following Sha et al. (2021). Further quantitative evaluation of the model results also used the TROPOMI measurements of HCHO and surface observation of O_3 and NO_2.

2.5 GEOS-Chem model experiments

A series of sensitivity experiments is conducted over China with different NOx and VOC emissions and GEOS-FP meteorological fields in different years using GEOS-Chem (v12.7.2) model. All simulations are conducted from Jan. 15 to Mar. 31. The 17 days before Feb. 1 are used for spin up, and the model output for Feb. and Mar. are used for the analysis. The configurations of different simulations are listed in Table 1.

Table 1. Configurations of model sensitivity experiments.

Experiments	Abbreviation	Meteorology	NOx Emission	VOC Emission
Baseline (2019)	2019B	GEOS-FP 2019	MIX 2019	MIX 2019
2020 Default	2020D	GEOS-FP 2020	MIX 2019	MIX 2019
2020 NOx	2020N	GEOS-FP 2020	MIX 2020	MIX 2019
2020 VOC	2020V	GEOS-FP 2020	MIX 2019	MIX 2020
2020 Lockdown	2020L	GEOS-FP 2020	MIX 2020	MIX 2020
2020 Adjoint	2020A	GEOS-FP 2020	Adjoint 2020	MIX 2020

We use the following equations to quantify the contributions from NOx and VOC emission reduction due to COVID-19 and meteorological variation to the increase of surface O_3.

$$\Delta O_3^{\mathrm{NOx}} = \frac{O_3^{2020\mathrm{A}} - O_3^{2020\mathrm{V}}}{O_3^{2019\mathrm{B}}} \times 100\% \quad (2)$$

$$\Delta O_3^{\mathrm{VOC}} = \frac{O_3^{2020\mathrm{L}} - O_3^{2020\mathrm{N}}}{O_3^{2019\mathrm{B}}} \times 100\% \quad (3)$$

$$\Delta O_3^{\mathrm{ems}} = \frac{O_3^{2020\mathrm{A}} - O_3^{2020\mathrm{D}}}{O_3^{2019\mathrm{B}}} \times 100\% \quad (4)$$

$$\Delta O_3^{\mathrm{met}} = \frac{O_3^{2020\mathrm{D}} - O_3^{2019\mathrm{B}}}{O_3^{2019\mathrm{B}}} \times 100\% \quad (5)$$

Where $\Delta O_3^{\mathrm{NOx}}$, $\Delta O_3^{\mathrm{VOC}}$ and $\Delta O_3^{\mathrm{ems}}$ are the relative differences in surface O_3 concentration caused by emission decline of NOx, VOC, and both NOx and VOC resulting from COVID-19. $\Delta O_3^{\mathrm{met}}$ represents the relative contribution to the surface O_3 change from the meteorological variation between 2 years. $O_3^{2019\mathrm{B}}$, $O_3^{2020\mathrm{D}}$, $O_3^{2020\mathrm{N}}$, $O_3^{2020\mathrm{V}}$, $O_3^{2020\mathrm{L}}$ and $O_3^{2020\mathrm{A}}$ are mean MDA8 surface O_3 concentration simulated by modeling experiments Baseline (2019), 2020 Default, 2020 NOx, 2020 VOC, 2020 Lockdown and 2020 Adjoint, respectively (Table 1).

The difference in simulated surface O_3 between 2020 and 2019, is the result of both emission reductions and meteorological variations and is denoted as $\Delta O_3^{\mathrm{all}}$. It is calculated as follows and is evaluated against the observed relative difference of mean MDA8 O_3 in Feb. to Mar. between 2019 and 2020 at all ground sites:

$$\Delta O_3^{\mathrm{all}} = \frac{O_3^{2020\mathrm{A}} - O_3^{2019\mathrm{B}}}{O_3^{2019\mathrm{B}}} \times 100\% \quad (6)$$

3. Results of model development, emissions, and validation

3.1 Changes of NOx and VOC emissions during COVID

We updated the anthropogenic NOx emissions during the COVID lockdown using both 4D-Var and mass balance methods (Fig. 1 and 2). The NOx emissions from the 4D-Var inversion share a similar spatial pattern and magnitude with those found using the mass balance method (Fig. 1). However, the NOx emissions from the 4D-Var inversion are lower overall than those from the mass balance method over North China by ~10% and larger over central China by ~40%. Fig. 2(a-b) shows that the 4D-Var NOx emission reduction is more severe over urban regions and displays a smoother spatial pattern than that from the mass balance approach, which is caused by the arbitrary cut off with 0.1 DU of NO_2 VCD in the latter. Furthermore, the 4D-Var inversion captured the NOx emission decline in Northeast China where the mass balance approach did not because of the low NO_2 VCD. During Feb.-Mar. 2020, the anthropogenic NOx emissions in East China decreased by ~30% compared to those in the same period in 2019.

We also scale the anthropogenic VOC emissions based on the TROPOMI HCHO data (Fig. 2(c)). The VOC emissions decrease by ~20%-30% in East and South Asia. The anthropogenic VOC emission changes in sparsely populated areas over Northwest China are neglected. TROPOMI HCHO data cannot distinguish the anthropogenic emissions from biogenic and biomass burning sources for the Indochinese Peninsula in Southeast Asia because of the dense

vegetation in this region. However, this study investigated the O_3 pollution in China, the Southeast Asia with the dense vegetation is out of our study domain. The impact of VOC emission bias in Southeast Asia on the surface O_3 pollution in China is negligible considering the lifetime of biogenic VOC is generally short (Atkinson, 2000). For the populated urban regions in China, where the surface O_3 pollution exerts more significant health impacts, the anthropogenic source dominates the VOC emissions (Williams and Koppmann, 2007).

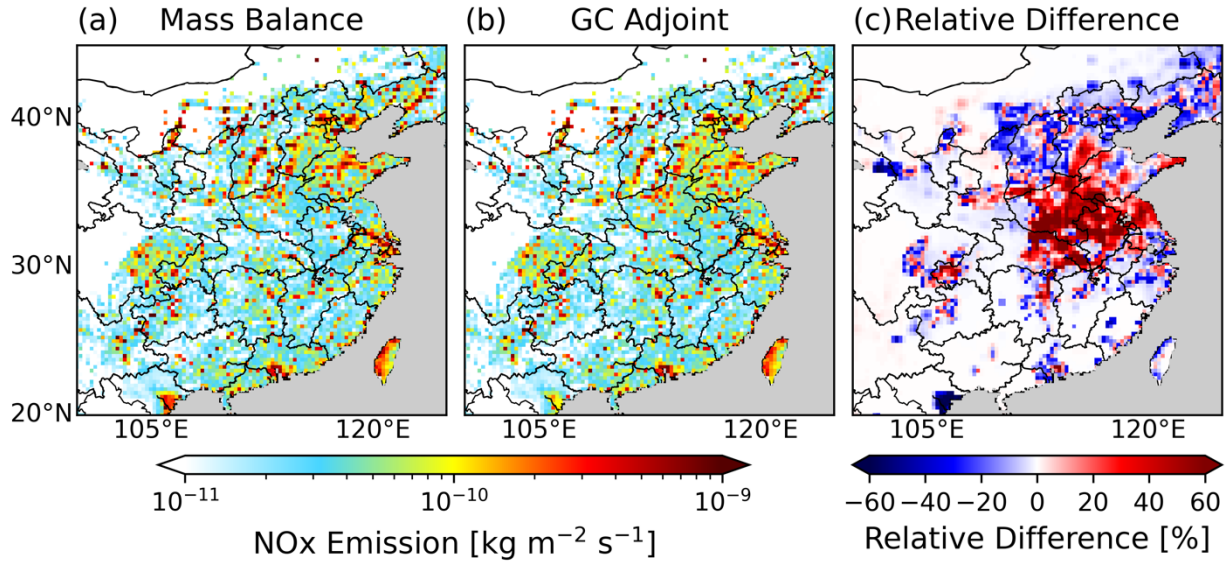

Figure 1. Updated anthropogenic NOx emission during Feb.-Mar. 2020 from (a) mass balance method, (b) 4D-Var method and (c) their relative difference. The relative difference is calculated as dividing the difference of (b) minus (a) by (a).

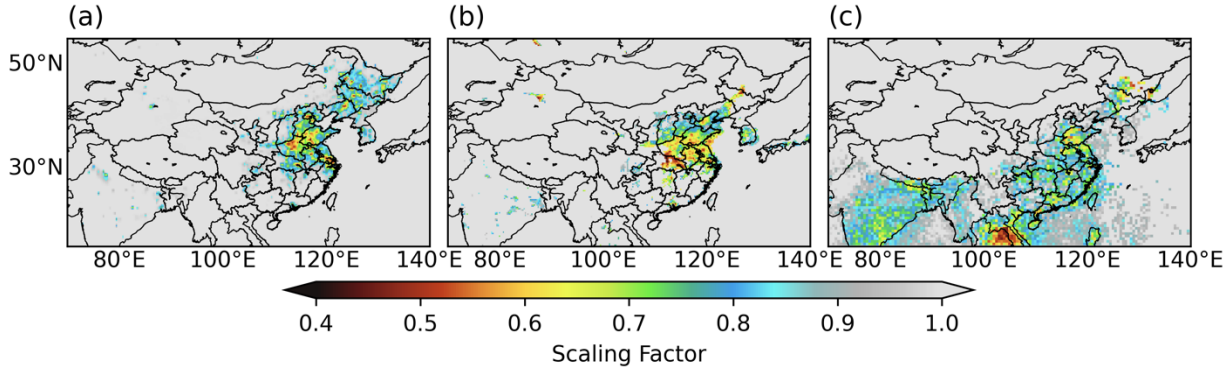

Figure 2. Scaling factors for anthropogenic NOx emission in Feb.-Mar. from 2019 to 2020 as derived from (a) 4D-Var, (b) mass balance. Scaling factors for anthropogenic VOC emissions from the mass balance are in (c).

3.2 Validation of NO_2 simulations

We further assess our updated anthropogenic NOx emissions by comparing the NO_2 VCD from TROPOMI with that from GEOS-Chem with the anthropogenic NOx emissions before and after the scaling (Fig. 3 and 4). Before updating the NOx emissions, the 2020 Default (Fig. 3(b)) simulation significantly overestimates the NO_2 VCD compared to the TROPOMI NO_2 observations (Fig. 3(a)). With the NOx emissions updated, the simulations 2020 NOx (Fig. 3(c)) and 2020 Adjoint (Fig. 3(d)) exhibit a much better agreement with TROPOMI NO_2 observation than 2020 Default. However, Fig. 3(c) shows the GEOS-Chem simulation with the NOx emissions from mass balance approach overestimated the NO_2 VCD over Beijing and southwest of Hebei Province (pink and black circles in Fig.3) compared with TROPOMI data. The reason is that scaling factors are applied only to anthropogenic NOx emissions, not total NOx emissions, so it is expected that the model may still overestimate the NO_2 column after scaling part of the total NOx emission. With the anthropogenic NOx emissions optimized by the 4D-Var method, the overestimation of NO_2 VCD over Beijing and southwest of Hebei Province (pink and black circles in Fig. 3) is mitigated compared with the NOx emissions from mass balance approach.

Fig. 4 further displays the statistics for the comparison between the TROPOMI NO_2 and GEOS-Chem simulations via the scatterplot. The Baseline (2019) simulation captures the magnitude of NO_2 VCD observations in 2019 well (Fig. 4(a)). The root-mean-square-error (RMSE) and mean bias error (MBE) for the simulation with 2020 NOx emission derived from mass balance method (Fig. 4(b)) decreased by 0.050 DU and 0.057 DU as compared to the 2020 Default (Fig. 4(c)). Compared with the result from GEOS-Chem simulation 2020 NOx, emissions from 2020 Adjoint (Fig. 4(d)) further led to the reduction of the MBE of the NO_2 VCD by 0.006 DU and improve the correlation coefficient by 0.003. The significant overestimation of several pixels with TROPOMI NO_2 VCD larger than 0.4 DU by the simulation 2020 NOx is also mitigated by 2020 Adjoint. The MBE between GEOS-Chem and TROPOMI for Baseline (2019), 2020 NOx and 2020 Adjoint are -0.004, 0.015 and 0.009 DU, respectively. The corresponding relative bias are 1.9%, 10% and 6.0%, which are all less than the relative uncertainty of ~30% for TROPOMI tropospheric NO_2 VCD over East China (Van Geffen et al., 2022). The improved agreement between the simulation with updated NOx emission and TROPOMI NO_2 provides a basis for further analyzing the mechanism of aggravated surface O_3 pollution.

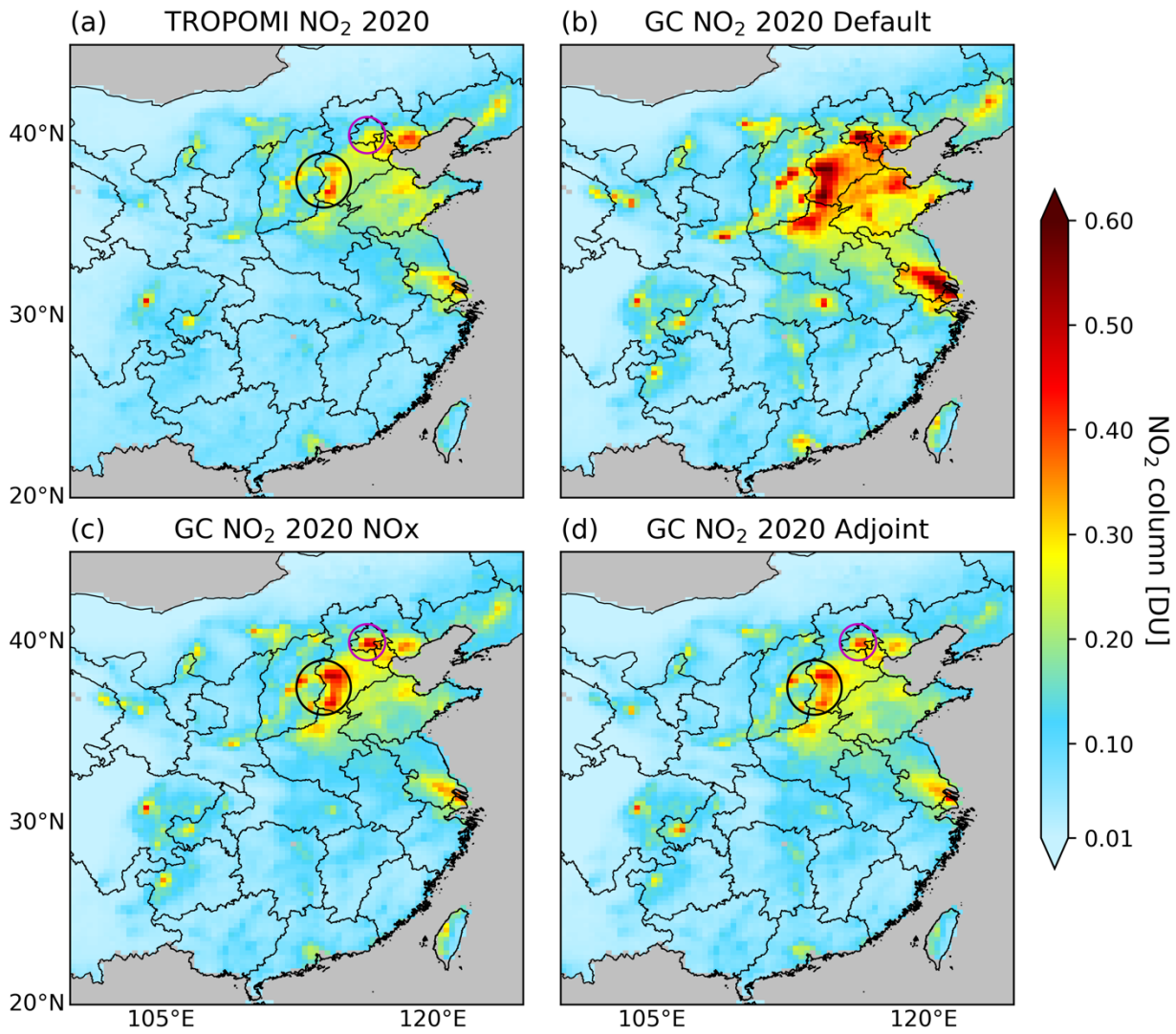

Figure 3. Comparison of tropospheric NO_2 VCD from (a) TROPOMI product in 2020 Feb.-Mar with that from GEOS-Chem simulations (b) 2020 Default, (c) 2020 NOx and (d) 2020 Adjoint. The pink and black circles mark the areas where NOx emissions from 4D-Var mitigated the NO_2 overestimation by mass balance method. The emissions and meteorology configurations for GEOS-Chem simulations 2020 Default, 2020 NOx and 2020 Adjoint are listed in Table 1.

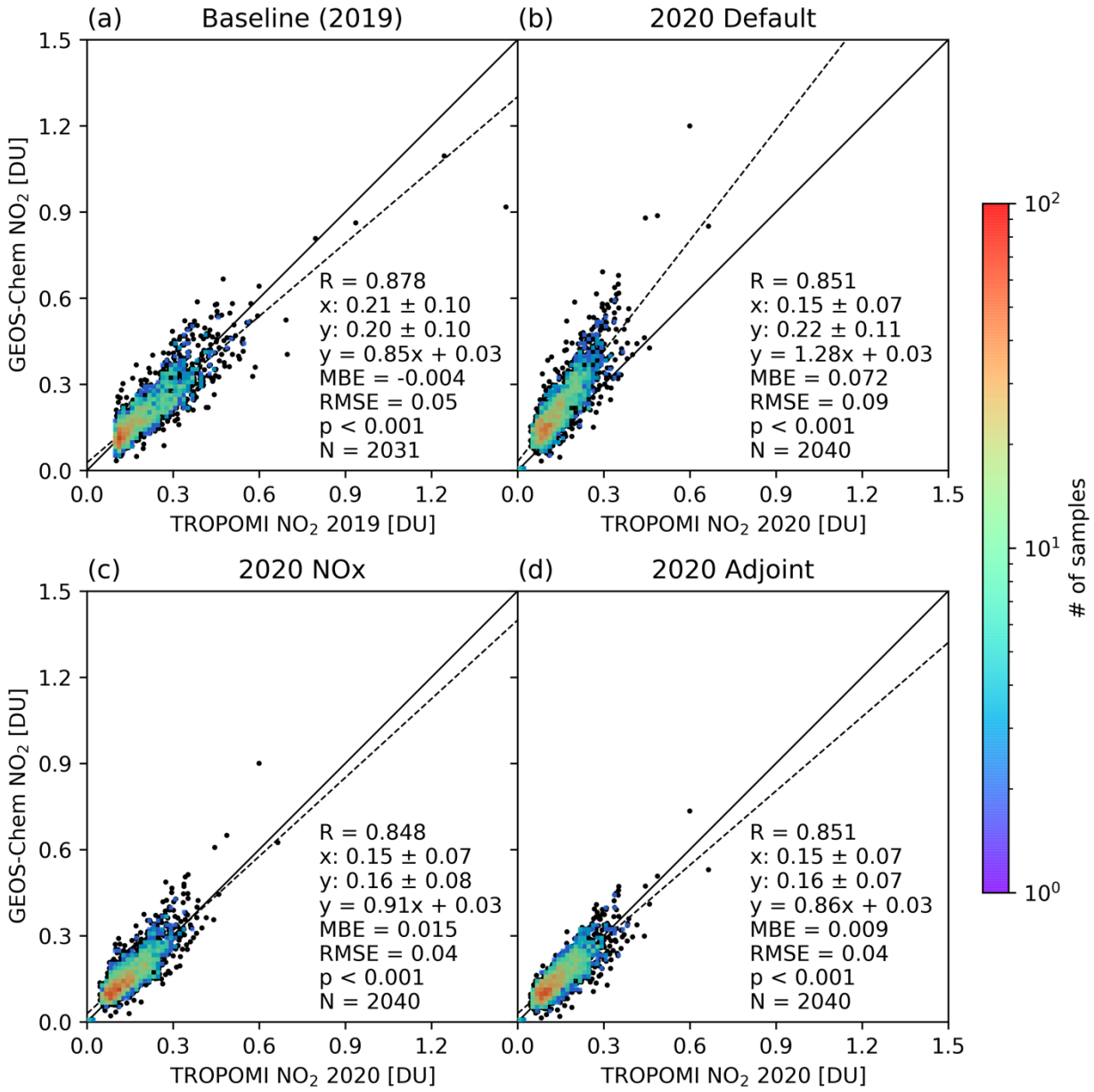

Figure 4. Scatter plot of TROPOMI NO_2 VCD versus the GEOS-Chem simulations for (a) Baseline (2019), (b) 2020 Default, (c) 2020 NOx and (d) 2020 Adjoint, respectively. TROPOMI data in Feb.-Mar. of 2019 was used in (a), and that of 2020 was used in (b-d). The emissions and meteorology configurations for GEOS-Chem simulations are listed in Table 1. Only pixels with TROPOMI NO_2 VCD in 2019 Feb.-Mar. larger than 0.1 DU are included in all comparisons.

Fig. 5 and Fig. 6 show the comparison of surface NO_2 between ground measurements and GEOS-Chem simulations. The GEOS-Chem simulations Baseline (2019) (Fig. 5(b)) and 2020 Adjoint (Fig. 5(d)) both capture the spatial pattern and magnitude of surface NO_2 measurements in Feb.-Mar. of 2019 (Fig. 5(a)) and 2020 (Fig. 5(c)) well, respectively. Fig. 6 further displays the good agreements of surface NO_2 from Baseline (2019) (Fig. 6(a)) and 2020 Adjoint (Fig. 6(b)) to the in-situ measurements via scatter plots. Table 2 displays the evaluation statistics, including the correlation coefficient (R), MBE, RMSE and the slope and intercept of the linear regression, for the simulated surface NO_2 from various simulation experiments compared with the in-situ measurements. The correlation coefficient, MBE and RMSE between the simulation Baseline (2019) and ground measurements in 2019 Feb.-Mar. are 0.724, 1.572 μg m^{-3} and 8.49 μg m^{-3}, respectively. Without updating the NOx emissions in 2020, the simulation 2020 Default overestimate the ground measurements of surface NO_2 in 2020 Feb.-Mar (Table 2). The slope for the linear regression is 1.19, and the MBE and RMSE are 6.021 μg m^{-3} and 10.43 μg m^{-3}, respectively (Table 2). After updating the NOx emissions, the GEOS-Chem simulations 2020 NOx and 2020 Adjoint have good agreements with the in-situ measurements in 2020 Feb.-Mar. The correlation coefficient between the simulation 2020 Adjoint versus the in-situ measurements is 0.651, higher than that of 0.608 for the simulation 2020 NOx versus the ground measurements (Table 2). The MBE and RMSE of 2020 Adjoint (0.683 μg m^{-3} and 6.68 μg m^{-3}) are lower than those of 2020 NOx (1.726 μg m^{-3} and 7.74 μg m^{-3}) (Table 2). This result further indicates the superiority of 4D-Var for optimizing NOx emissions compared with the mass balance method (Cooper et al., 2017; Streets et al., 2013).

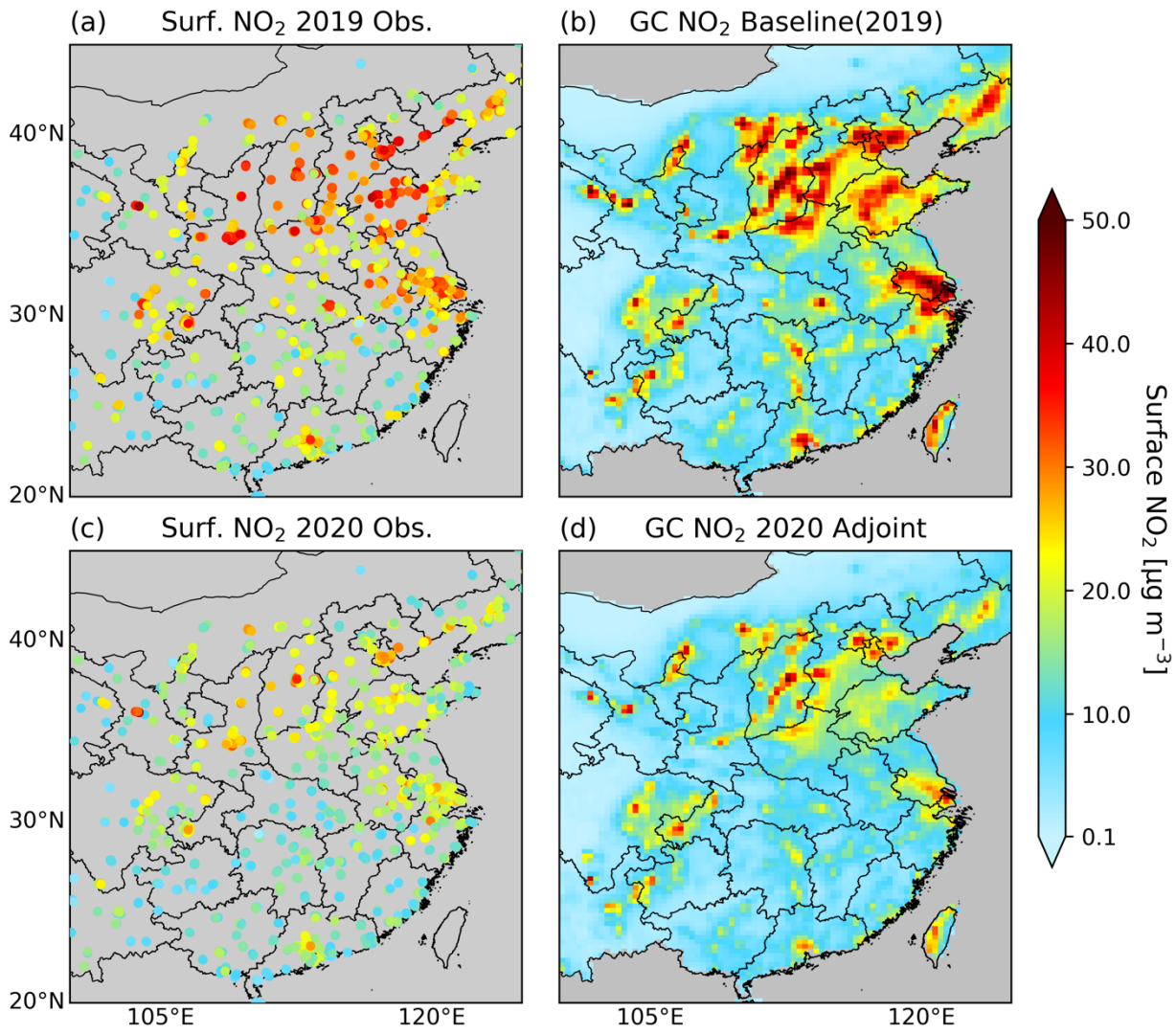

Figure 5. Comparison of surface NO_2 concentrations from ground measurements for (a) 2019 Feb.-Mar. and (c) 2020 Feb.-Mar. versus those from GEOS-Chem simulations (b) Baseline (2019) and (d) 2020 Adjoint. Grey color means no data is presented.

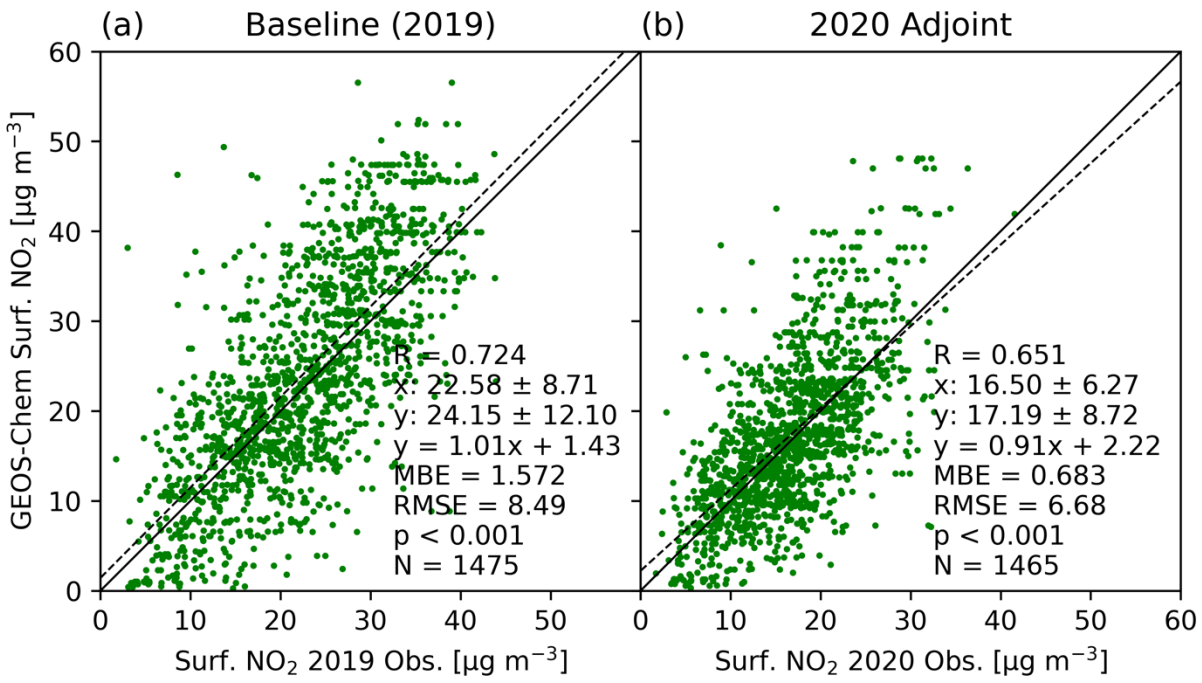

Figure 6. Scatter plots for comparing the surface NO_2 concentrations from GEOS-Chem simulations and ground measurements. (a) GEOS-Chem simulation Baseline (2019) versus ground measurements in 2019 Feb.-Mar. (b) GEOS-Chem simulation 2020 Adjoint versus ground measurements in 2020 Feb.-Mar. Note: the number of ground sites differ in these two years.

Table 2. Evaluation statistics for modeled surface NO_2 compared with the in-situ measurements*.

Experiments	R	MBE (μg m^{-3})	RMSE (μg m^{-3})	Slope	Intercept (μg m^{-3})
Baseline (2019)	0.724	1.572	8.49	1.01	1.43
2020 Default	0.661	6.021	10.43	1.19	2.95
2020 NOx	0.608	1.726	7.74	0.92	3.03
2020 Adjoint	0.651	0.683	6.68	0.91	2.22

* The simulation experiment Baseline (2019) is compared with the ground measurements in 2019 Feb.-Mar. Other three experiments are compared with the ground measurements in 2020 Feb.-Mar.

Fig. 7 (a) is the Taylor diagram for evaluating the GEOS-Chem simulations of surface NO_2 concentrations from 2020 Default, 2020 NOx and 2020 Adjoint using the in-situ measurements.

The simulation 2020 Adjoint (inverted triangle in Fig. 7(a)) has the best performance among these three simulations with the lowest relative bias and lowest normalized centered RMSE. Without updating the NOx emission, 2020 Default features a relative bias of ~37%. After updating the NOx emissions, 2020 NOx reduces the relative bias, normalized centered RMSE and normalized standard deviation from around 37%, 1.38 and 1.80 to around 10%, 1.20 and 1.51 compared with 2020 Default, but the correlation coefficient also decreases. By using 4D-Var method, 2020 Adjoint further reduces the relative bias, normalized centered RMSE and normalized standard deviation and increases the correlation coefficient compared with 2020 NOx. We also validated the VOC emissions by comparing the simulated HCHO VCD with TROPOMI measurements (Appendix D).

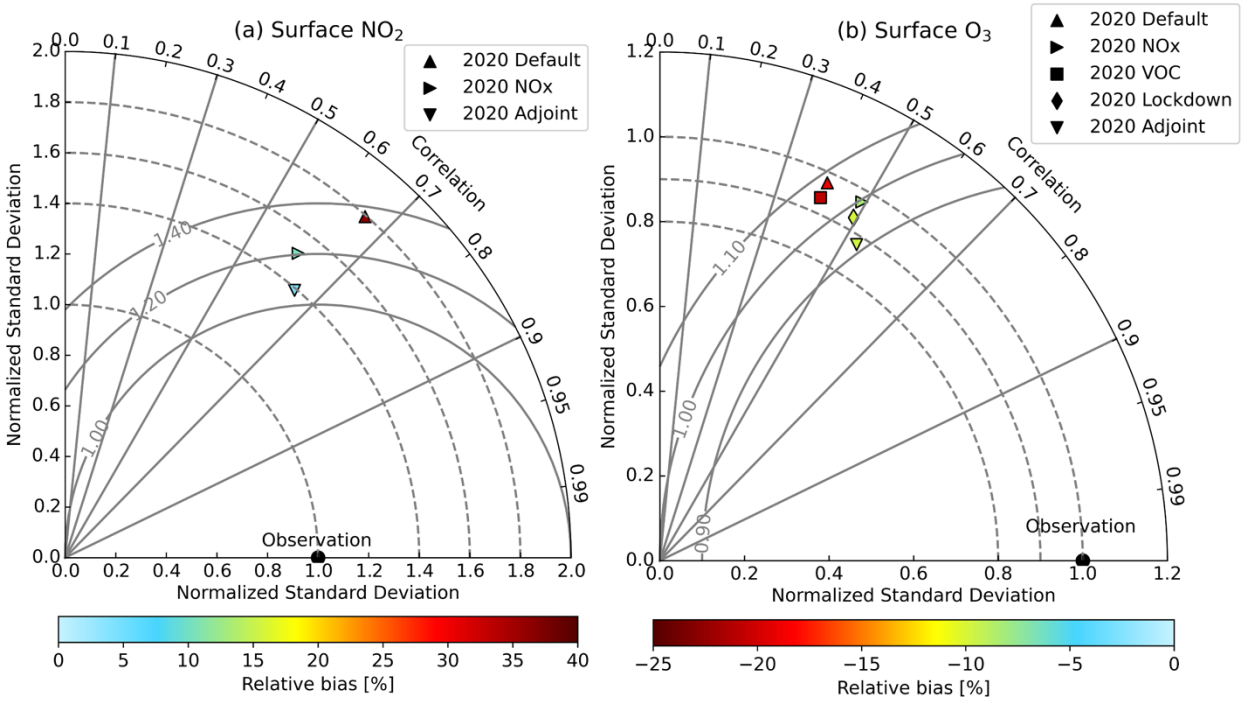

Figure 7. Taylor diagram for evaluating the GEOS-Chem simulations of (a) surface NO_2 and (b) surface O_3 during lockdown period (2020 Feb.-Mar.) using ground observations for different simulation experiments listed in Table 1. The evaluation of surface O_3 only includes the areas where the NOx emissions optimized by 4D-Var reduced by more than 10%.

3.3 Evaluation of surface O_3 simulations

We evaluated the GEOS-Chem simulations of MDA8 surface O_3 from different simulation experiments listed in Table 1 using ground measurements. Fig. 7(b) is the Taylor diagram for comparing the surface O_3 concentrations during 2020 Feb.-Mar. from ground measurements and GEOS-Chem simulations. We focused on areas with significant NOx emissions reduction to better assess the role of updated NOx emissions in improving surface O_3 simulations. The ground sites where the NOx emissions from 4D-Var decline by less than 10% are excluded. The correlation coefficient between the simulation Baseline (2019) and ground observations is ~0.53 and the relative bias is around -25%. By applying 2020 meteorological fields and scaling the VOC emissions, the correlation coefficients decreased to ~0.40 for model simulations 2020 Default and 2020 VOC, with little reduction in the relative bias. By updating the NOx emissions, the relative bias reduced to around -10% while the correlation coefficients remain at ~0.50 for model simulations 2020 NOx, 2020 Lockdown and 2020 Adjoint. This indicates the NOx emission updates significantly improve the surface O_3 simulations. Comparing the simulations 2020 Default and 2020 VOC, or 2020 NOx and 2020 Lockdown, the results show that scaling VOC emissions does not improve the surface O_3 simulations significantly over the continental China, but over South China, VOC emissions update reduces the relative bias by 3%. Among all simulations, 2020 Adjoint exhibits the best performance with the lowest normalized centered RMSE, largest correlation coefficient and a low relative bias of ~10%. This result further confirms the superiority of the 4D-Var with respect to the mass balance method for optimizing NOx emissions. Therefore, we used the 2020 Adjoint to evaluate the impacts of NOx emission on surface O_3 in the following analysis.

Fig. 8 compares the modeled surface O_3 in Feb.-Mar. of 2019 (Fig. 8(a)) and 2020 (Fig. 8(b)) and the relative difference (Fig. 8(c)) computed from Equation (6) with the in-situ measurements (Fig. 8(d-f)). The ground observations show that the highest level of surface O_3 pollution occurs in North China and southwest of China. The average MDA8 O_3 in two months can reach up to ~110 μg m^{-3} at STP (~51.4 ppbv), which is higher than the China National Ambient Air Quality Standard daily maximum 8-hour Grade I standard of 100 μg m^{-3}. GEOS-Chem model underestimates the surface O_3 over North China for both years compared with ground observations, which could be a result of the underestimation of biogenic~~out-of-date~~ VOC emissions (Appendix D). The underestimation of the simulated O_3 over North China will not significantly affect our study purpose since this study focuses on revealing the impacts of emissions and meteorology

change on the surface O_3 change by each region. The bias is predominantly systematic and will be substantially cancelled when we compute the relative difference of the surface O_3. ~~,~~ The model~~but it~~ captures the magnitude and spatial distribution of surface O_3 and the increasing trend in South China well. In South China, the measured surface O_3 in 2020 Feb.-Mar. increases by 30-50%, while over North China, it increases generally by less than 20% even decreases in some regions. The relative differences of simulated surface O_3 between two years is comparable to the ground observations over South China (green box in Fig. 8(c, f)). In Sichuan Basin, the trend of the surface O_3 change from the model is opposite to the measurements, which is probably caused by the inaccurate simulation of the meteorological effects (See Section 4.1) due to the complex terrain features in this region. The localized improvement of the model simulation is further needed for the regional study. Over North China (pink box in Fig. 8(c, f)), the average relative difference between two years from the model and observation are 4.27% and -3.01%, respectively, both of which are much smaller than their counterparts in South China. While the relative difference from model simulations has different signs as compared to that of observations on average, both the change of O_3 is indeed small and the model is able to capture the part of O_3 decrease in the southwest part of the North China domain (Fig. 8(c)). We note that some previous studies showed large increase of O_3 in North China, but such increase is in comparison with the O_3 in the month right before the lockdown (not the same time in 2019; (Shi & Brasseur, 2020; Y. M. Liu et al., 2021).

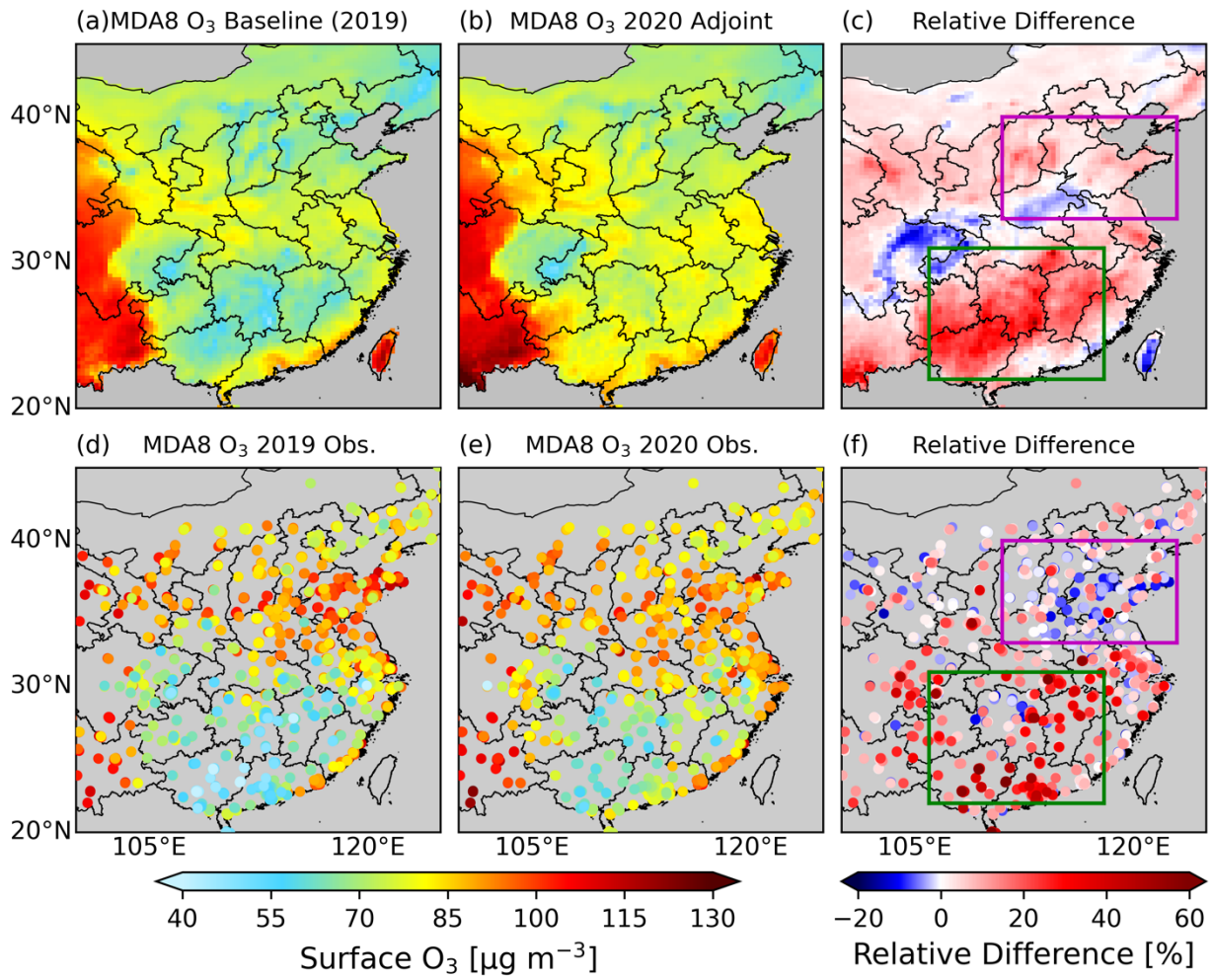

Figure 8. Comparison of MDA8 surface O_3 in 2019 and 2020 Feb.-Mar. and the relative difference between two years from GEOS-Chem model (a-c) versus ground observations (d-f). GEOS-Chem mean MDA8 O_3 at 9 m above the surface under standard temperature and pressure (STP; 273.15 K, 101.325 kPa) from (a) Baseline (2019) and (b) 2020 Adjoint simulation (Table 1) together with (c) their relative difference. Ground observed mean MDA8 surface O3 under STP in (d) 2019 Feb.-Mar.; (e) 2020 Feb.-Mar. and (f) their relative difference. The pink and green boxes in (c) and (f) define the North China and South China domain.

4. Mechanism of aggravated surface O_3 pollution

4.1 Relative contribution from declining emissions and meteorological variations

From equations (2)-(5) we can analyze the mechanism of surface O_3 increase in China during the COVID-19 pandemic (Fig. 9). NOx emission reduction as a result of COVID-19 lockdown leads to a ~8% increase in the mean MDA8 surface O_3 over North China (pink boxes in Fig. 9) between 2019 and 2020 Feb.-Mar. (Fig. 9(a)), while the VOC emission decline causes ~3% of O_3 decrease (Fig. 9(b)). The average contribution of the meteorological variations to the surface O_3 change is less than 1% in North China (Fig. 9(d)). However, in South China, the inter-annual meteorological variations dominate the surface O_3 increases, causing a ~30% increase (Fig. 9(d)), while the NOx and VOC emission reduction has little impacts. The overall magnitude of emissions contribution to the surface O_3 change over North China is ~5%, similar to that of the meteorological effects, but meteorological variations lead to both O_3 increases and decreases in different regions. Over South China, the meteorological effect is much larger than the net effects of declining emissions. Overall, the impact of inter-annual meteorological variations between 2019 and 2020 is almost 30 times larger than the overall emissions impacts on the aggregated surface O_3 pollution in China. Our results are consistent with the conclusion from Zhao et al. (2020) that meteorological variation has larger impacts than emissions reduction on surface O_3 in the southern city of Guangzhou, but in Beijing, emission reduction has a larger impact during 23-29 January. Liu et al. (2020b) reported that the surface O_3 increase in the major cites of the Yangtze River Delta region were driven by both emission reduction and meteorological variations to a similar degree from pre-lockdown period (Jan. 1-22, 2020) to lockdown period (Jan. 23-Feb. 29, 2020). However, Zhao et al. (2020) and Liu et al. (2020b) only focused on the lockdown period of one week in reference to the time period right before the lockdown instead of the same period in previous years, which cannot exclude the effects of seasonal variation of meteorology and did not provide a comprehensive analysis over the whole lockdown period. Moreover, Liu et al. (2020b) only analyzed four representative cities instead of showing the analysis at a national scale. Further, Zhao et al. (2020) did not update the anthropogenic emissions during the lockdown period, which brings significant uncertainties to their analysis. Previous studies found that TROPOMI NO_2 product has a negative bias of -7% to -20% (Verhoelst et al., 2021; Judd et al., 2020; Li et al., 2021). The sensitivity simulations indicate this low bias does not significantly affect the model evaluation and our main conclusions (figures not shown).

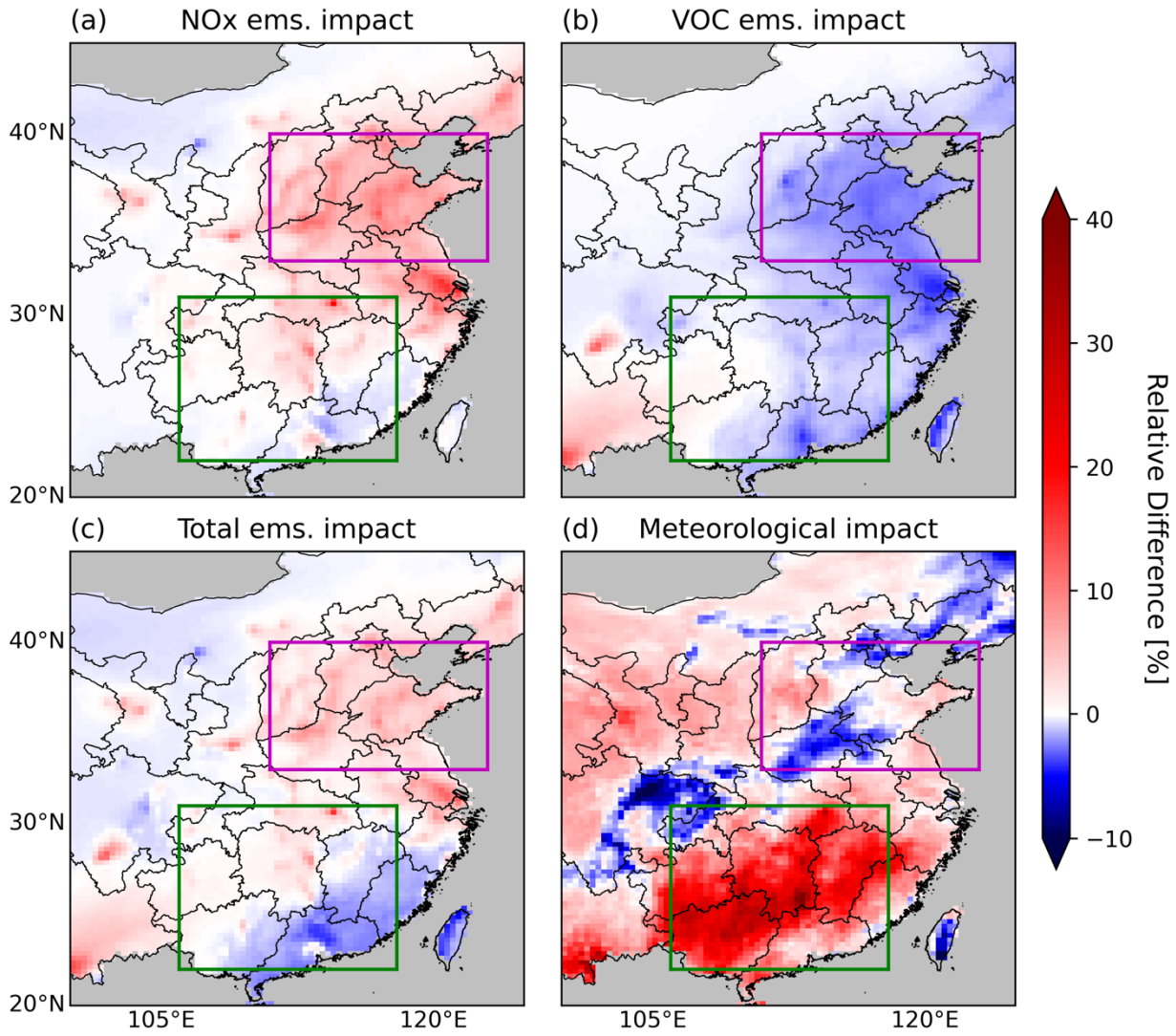

Figure 9. Relative difference in simulated surface O_3 caused by (a) NOx emission reduction, (b) VOC emission reduction, (c) overall emission reduction and (d) meteorological variations due to COVID-19 lockdown. The pink and green boxes in each panel define the North China and South China domain.

4.2 Critical meteorological variables~~Higher temperature~~ causing~~leading to~~ aggravated surface O_3 pollution in South China

To identify the critical meteorological variables that lead to the aggravated surface O_3 pollution in South China, we investigated the correlations between the surface O_3 concentrations and 2-m air temperature, downward visible direct flux at surface, cloud fraction, relative humidity,

and wind speed. The positive correlation between the surface O_3 and temperature is widely observed and reported in the literature (Pusede et al., 2015). Higher temperature leads to higher concentrations of surface O_3 because it improves the O_3 production rate by affecting the organic reactivity, production of HOx radicals, formation and decomposition of peroxy nitrates and alkyl nitrates (Pusede et al., 2015). We calculated the daily difference in Feb.-Mar. between 2020 and 2019 (excluding Feb. 29, 2020) for the daily mean of MDA8 O_3 from ground measurements and 2-meter air temperature, downward visible direct flux at surface and cloud fraction from GEOS-FP data used in our GEOS-Chem simulations for the South China (106°E - 118°E, 22°N - 31°N, green box in Fig. 10(a-c)) and North China (111°E - 123°E, 33°N - 40°N, pink box in Fig. 10(a-c)). Fig. 10 displays the difference of 2-month mean 2-meter air temperature (Fig. 10(a)), downward visible direct flux at surface (Fig. 10(b)) and cloud fraction (Fig. 10(c)) in Feb.-Mar. between 2020 and 2019 ~~(Fig. 10(a))~~ and the scatter plot between the daily difference of measured surface O_3 concentration and 2-meter air temperature (Fig. 10(d)), ~~-~~downward visible direct flux at surface (Fig. 10(e)) and cloud fraction (Fig. 10(f)) over both South China (green dots in Fig. 10(d-f~~b~~)) and North China (pink dots in Fig. 10(d-f~~b~~)). We found the 2-meter air temperature increased by ~2.3°C in South China, and the daily difference of surface O_3 concentration and 2-meter air temperature are well correlated with a positive correlation coefficient of 0.612. Therefore, the temperature increase contributed to the significant aggravated surface O_3 pollution in South China ~~could be attributed to the temperature increase~~. The enhanced solar radiation at ~~the~~ surface could also promote the production of O_3 via photochemical reactions. The correlation coefficient between the daily difference of surface O_3 concentration and downward visible direct flux at surface is as high as 0.740 in South China (Fig. 10(e)). The reason for the increase of temperature ~~increase~~ and solar radiation at surface is the lower cloud fraction. Via analyzing the GEOS-FP data, we found the cloud fraction decreases by ~5% (Fig. 10(c)), and the downward visible direct flux at surface increased by 5 W m^{-2} (Fig. 10(b)) over South China. The lower cloud fraction increases the downward solar radiation at the surface during the lockdown period, leading to higher surface air temperature. The change of cloud fraction is negatively correlated with the change of surface O_3 in South China with the correlation coefficient of -0.619 (Fig. 10(f)).

~~The enhanced solar radiation at the surface could also promote the production of O_3 via photochemical reactions.~~ In North China, 2-meter air temperature also increased by 1.8°C, but the measured surface MDA8 O_3 decreased by 3% (Fig. 8(f)). Fig. 10(d~~b~~) shows the daily difference

of MDA8 O_3 and 2-meter air temperature over North China also has a high correlation coefficient of 0.731. However, the intercept of the linear regression line is negative, so that the surface O_3 could decrease even though the temperature increases. This negative intercept is caused by the net effects of factors other than temperature, including chemistry, emissions, and other meteorological factors. It is a challenge to quantify the contributions of each individual factors, because these factors are thermodynamically or dynamically related. The predicted average change of surface MDA8 O_3 in South China and North China are marked by the green and pink open squares respectively in Fig. 10(d~~b~~) based on the linear regression. Because of the different intercepts, the predicted MDA8 O_3 in South China increases by ~9.0 μg m^{-3}, while it decreases by 2.2 μg m^{-3} in North China, although the average temperature increased in both South and North China. On the contrary to South China, the change of solar radiation at surface and cloud fraction are poorly correlated with the change of surface O_3 concentrations in North China (Fig. 10(e, f)), mainly due to a more important role of emission change in regulating the surface O_3 in North China.

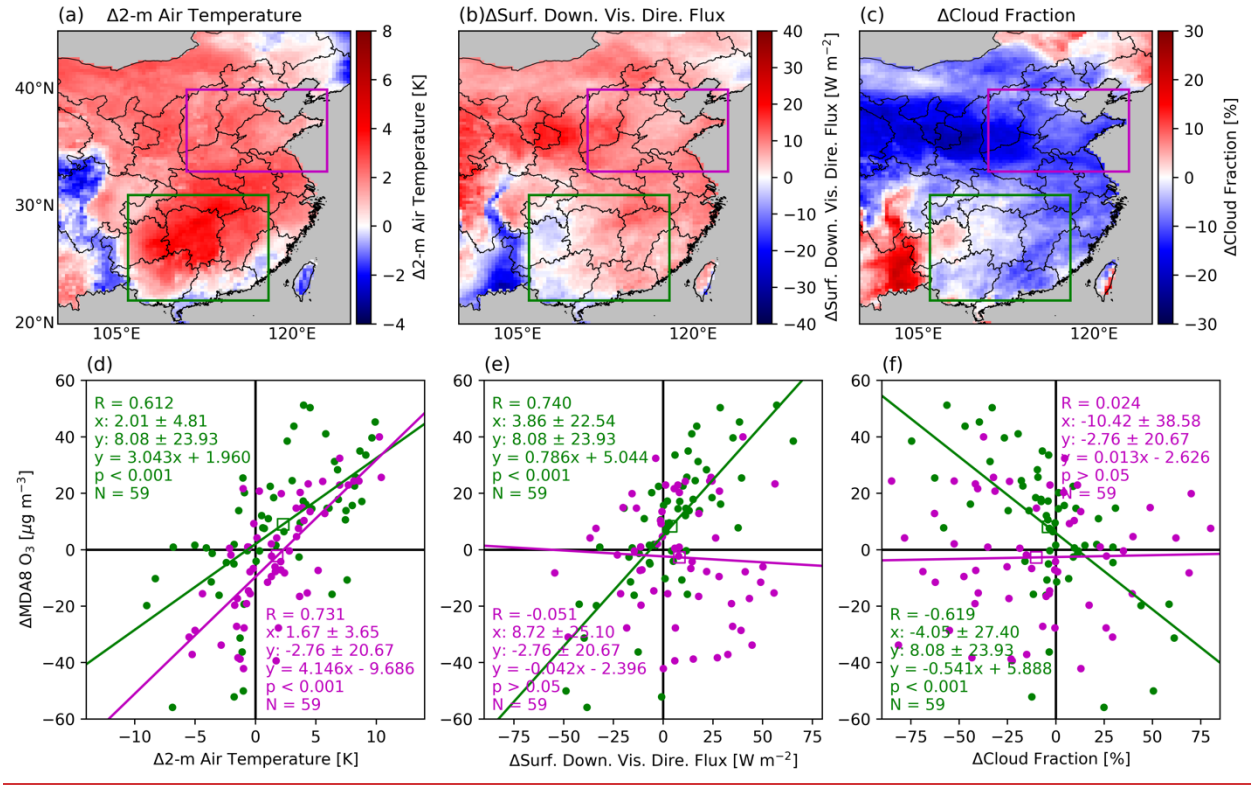

565

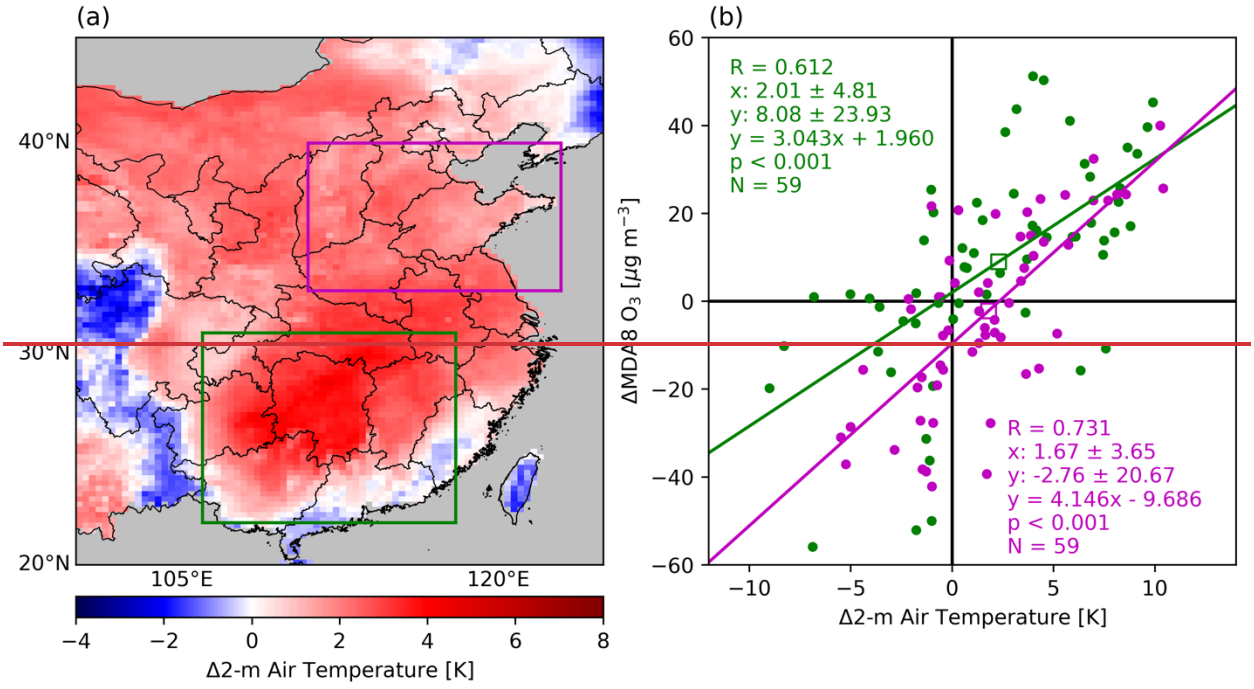

566

567 **Figure 10.** ~~(a)~~ The changes of (a) 2-meter air temperature, (b) downward visible direct flux at
568 surface and (c) cloud fraction from 2019 Feb.-Mar. to 2020 Feb.-Mar. ~~(b)~~ and t~~T~~he scatter plots
569 between the daily difference of surface O_3 measurements and (d) 2-meter air temperature, (e)

downward visible direct flux at surface and (f) cloud fraction in Feb.-Mar. between 2020 and 2019 over South China (green dots) and North China (pink dots). The green and pink open squares in (d-f) mark the predicted average change of surface MDA8 O_3 in South China ~~(green open square)~~ and North China ~~(pink open square)~~, respectively, based on the linear regression against ~~temperature~~the change of meteorological variables ~~change~~.

The impacts of relative humidity and wind speed on the surface O_3 change are also investigated (Fig. 11). The relative humidity increased by ~5.1% in North China and decreased by ~3.0% in South China on average. The strong correlation (R = -0.675) between the change of relative humidity and surface O_3 in South China indicates the decrease of relative humidity also contributes to the increase of surface O_3 pollution in South China, but the correlation between them in North China is very low. The wind speed also changed oppositely in South China and North China, but we cannot identify any significant impact of wind speed on the surface O_3 pollution since the correlation coefficients are low in both South China and North China. In summary, the significant increase of surface O_3 pollution during the lockdown period in South China could be primarily attributed to the higher temperature, enhanced solar radiation at surface and declined relative humidity.

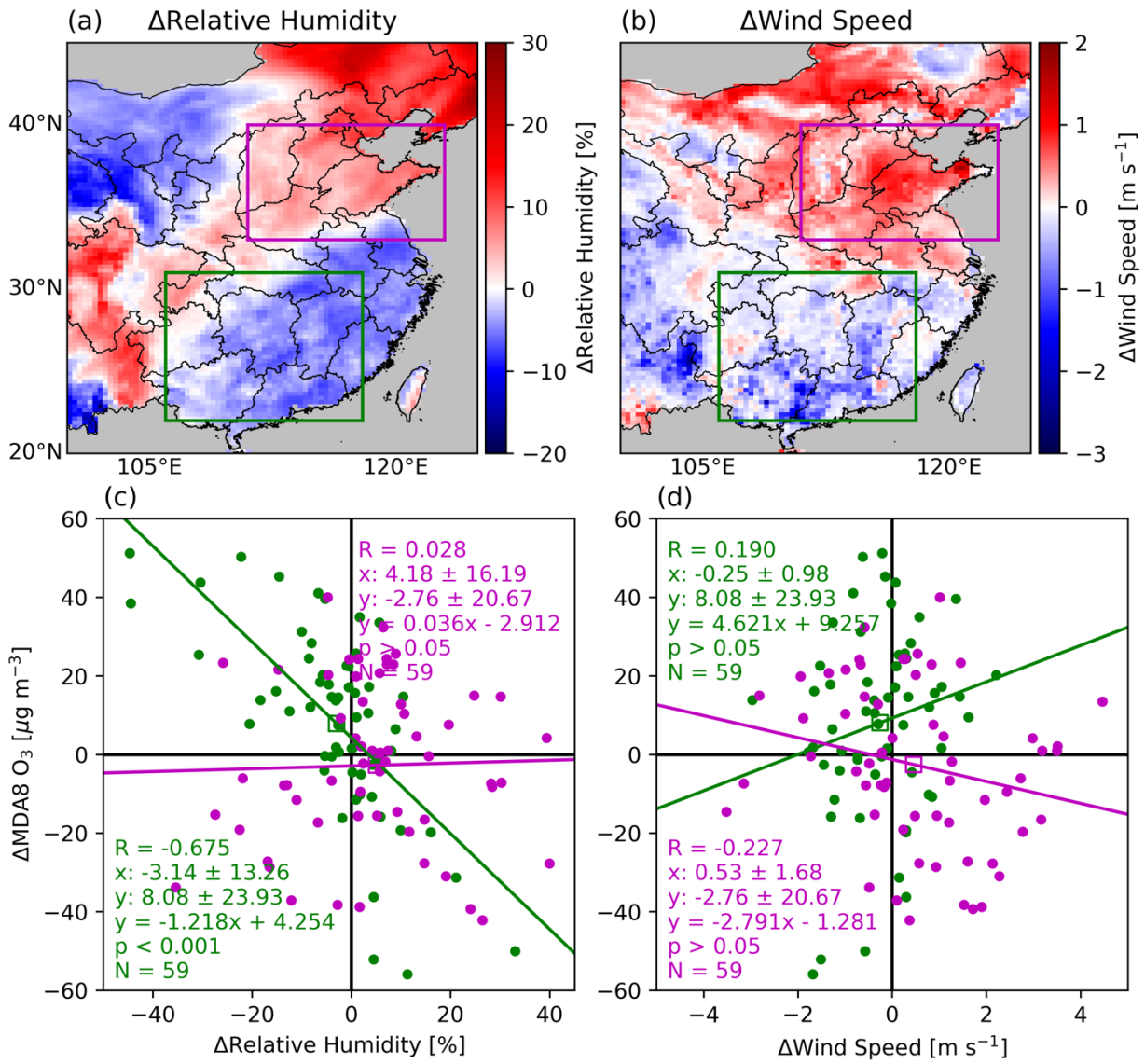

Figure 11. Same as Fig. 10 but for (a, c) relative humidity and (b, d) wind speed.

5. Summary

A significant reduction in primary air pollutants has been identified by surface and satellite observations during the COVID-19 pandemic in China (Bauwens et al., 2020; Miyazaki et al., 2020), which is in contrast to the increase of surface O_3. In this study, we analyzed the reasons for the enhanced surface O_3 pollution from two perspectives: anthropogenic emissions reduction and inter-annual meteorological variations. We constrain the NOx emissions based on the TROPOMI NO_2 product using both the mass balance and 4D-Var methods. The VOC emissions~~w~~ were also

updated based on the TROPOMI HCHO product via the mass balance approach. We analyzed the contributions from emissions reduction and meteorological variations to surface O_3 increases through a series of sensitivity simulations using the GEOS-Chem model.

The updated NOx emissions from the 4D-Var and mass balance approaches share a similar spatial pattern. However, the NOx emissions from 4D-Var are lower than those from the mass balance method over North China by ~10% but larger over central China by ~40%. The evaluation of the simulations with the updated emissions against the TROPOMI NO_2, in-situ measurements of surface NO_2 and O_3 indicate that the NOx emissions from the 4D-Var inversion leads to better model performance than that from the mass balance approach.

The anthropogenic NOx emission decreased by ~30% over East China during 2020 Feb.-Mar. compared to the same period in 2019. Over North China, NOx emission reduction leads to a ~8% increase in the mean MDA8 surface O_3, while the VOC emissions decline causes O_3 to decrease by ~3%. The average contribution of meteorological variations to the surface O_3 change is less than 1% in North China. However, in South China, the inter-annual meteorological variation dominates the surface O_3 increase, causing a ~30% increase, while the NOx and VOC emission reduction has nearly no impacts on O_3. Overall, the impact of inter-annual meteorological variations between 2019 and 2020 is almost 30 times larger than the impact of emissions -on the enhanced surface O_3 pollution in China.

The significant increase of surface O_3 in South China could be attributed to the higher temperature, enhanced solar radiation at surface and declined relative humidity during the lockdown period.~~, which is caused by the lower cloud fraction.~~ The lower cloud fraction increases the downward solar radiation at the surface during the lockdown period, leading to higher surface air temperature. We cannot identify any significant impact of wind speed on the surface O_3 pollution.~~ The enhanced solar radiation at the surface could also promote the production of O_3 via photochemical reactions.~~

Appendix A: NOx emission reduction in China from 2010 to 2019

The default anthropogenic NOx emission over East Asia in GEOS-Chem is MIX 2010 (Li et al., 2017).To generate the anthropogenic NOx emission in 2019, we calculated the ratio of mean TROPOMI tropospheric NO_2 VCD in Feb.-Mar. 2019 to GEOS-Chem simulated NO_2 VCD with

the default MIX 2010 emission as the scaling factor (Fig. A1). The scaling factors in regions where mean TROPOMI tropospheric NO_2 VCD in 2019 Feb.-Mar. less than 0.1 DU are set to 1. From 2010 to 2019, the anthropogenic NOx emission has declined significantly as a result of the clean air actions of Chinese government (Zheng et al., 2018).

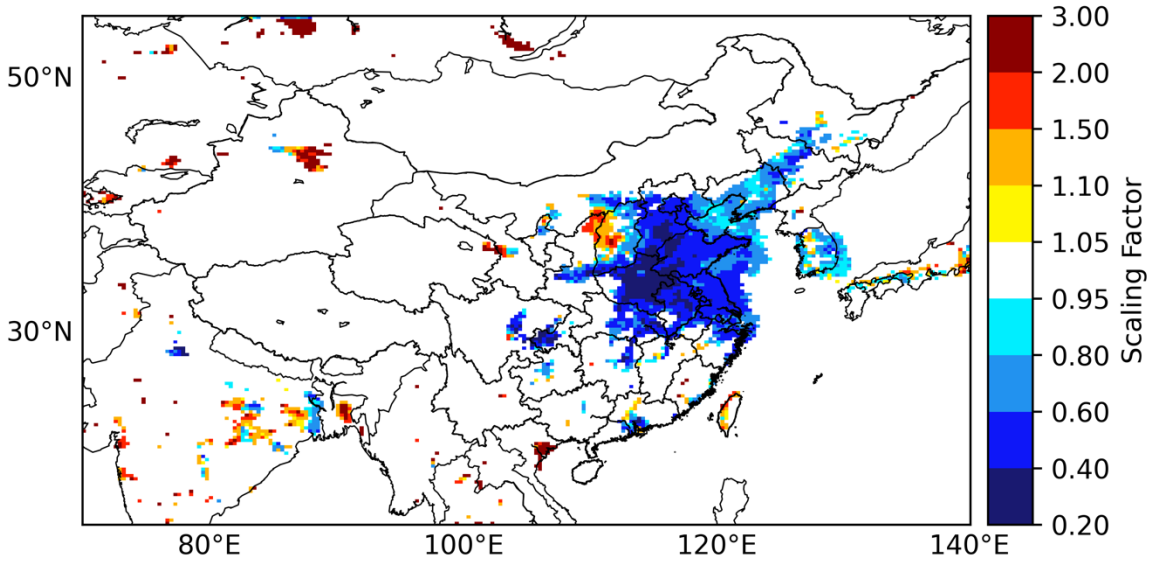

Figure A1. The scaling factor of anthropogenic NOx emission from year 2010 to 2019.

Appendix B: Applying the TROPOMI NO_2 averaging kernel in the observation operator

To optimize the NOx emissions and minimize the cost function (Equation (1)) with the 4D-Var method, GEOS-Chem adjoint needs to compute the derivative of the cost function with respect to the model parameters to be optimized, which is the scaling factors of the anthropogenic NOx emissions in this study. An essential step is to calculate the adjoint forcing $\boldsymbol{F}$, which is the derivative of the cost function with respect to the modeled NO_2 concentration shown as Equation (B1).

$$\boldsymbol{F} = \frac{\partial J}{\partial \boldsymbol{c}} = \boldsymbol{S}_{\text{obs}}^{-1}[H(\boldsymbol{c}) - \boldsymbol{s}]\frac{\partial H(\boldsymbol{c})}{\partial \boldsymbol{c}} \quad \text{(B1)}$$

For each single TROPOMI NO_2 observation, the adjoint forcing component f and cost function component j are computed as Equation (B2) and Equation (B3).

$$f = \frac{M_{gc} v_{gc} - M_{obs} v_{obs}}{e_{obs} M_{obs}} M_{gc} \quad \text{(B2)}$$

$$j = \frac{0.5 f \left(M_{gc} v_{gc} - M_{obs} v_{obs} \right)}{M_{gc}} \quad \text{(B3)}$$

Here M_{gc} is GEOS-Chem air mass factor applying the GEOS-Chem NO_2 vertical profiles and TROPOMI NO_2 averaging kernel. M_{obs} is TROPOMI air mass factor. v_{gc} and v_{obs} are the tropospheric NO_2 VCD from GEOS-Chem model and TROPOMI observation, respectively. The product of air mass factor and NO_2 VCD is NO_2 slant column density. e_{obs} is the standard error of TROPOMI tropospheric NO_2 VCD.

We calculated the GEOS-Chem air mass factor M_{gc} as Equation (B4) following Qu et al. (2019).

$$M_{gc} = \frac{\sum_{i \in \text{trop.}} c_i^{gc} \Delta p_i^{gc} w_i^{gc}}{\sum_{i \in \text{trop.}} c_i^{gc} \Delta p_i^{gc}} \quad \text{(B4)}$$

Here c_i^{gc} is GEOS-Chem NO_2 mixing ratio at vertical layer i, Δp_i^{gc} is the pressure difference between the GEOS-Chem vertical layer i and i+1. w_i^{gc} is the scattering weight at the GEOS-Chem vertical layer i, which is calculated by the linear interpolation of the scattering weights at the vertical coordinate of the model TM5 used for TROPOMI NO_2 retrieval. The scattering weight at the TM5 vertical layer l (w_l^{TM5}) is computed as the product of TROPOMI air mass factor and the TROPOMI averaging kernel at the TM5 vertical layer l (A_l^{TM5}) using Equation (B5-B6) (Eskes and Boersma, 2003; Palmer et al., 2001).

$$w_l^{TM5} = \frac{M_{obs} A_l^{TM5}}{M_{geo}} ~~M_{obs} A_l^{TM5}~~ \quad \text{(B5)}$$

$$M_{geo} = \sec \theta_0 + \sec \theta \quad \text{(B6)}$$

where M_{geo} is geometric air mass factor, θ_0 and θ are solar zenith angle and viewing zenith angle, respectively.

Appendix C: Validation of the TROPOMI NO_2 observation operator

We validated the observation operator by comparing the sensitivity of the cost function with respect to the emission scaling factor from GEOS-Chem adjoint and a finite difference estimation as shown in Equation (C1). We shut down the transport and exclude a priori term from

the cost function for the validation, so that the gradient of cost function component in each grid cell to the local emission scaling factor equals to the gradient of total cost function to the emission scaling factor in the same grid cell.

$$\frac{\partial J(\ln \sigma)}{\partial \ln \sigma} \approx \frac{J(\ln(\sigma + 0.05)) - J(\ln(\sigma - 0.05))}{\ln(\sigma + 0.05) - \ln(\sigma - 0.05)} \quad \text{(C1)}$$

Fig. C1 compared the cost function sensitivities calculated from GEOS-Chem adjoint and the finite difference method for the nested grids with the spatial resolution of 0.25°×0.3125°. The spatial pattern and magnitude of the cost function sensitivities from the two methods match with each other with a correlation coefficient of 0.97. The statistics show that the agreement of the adjoint sensitivities and finite difference sensitivities in this study is comparable to that in Wang et al. (2020a) although we constrain the NOx emission at a much finer resolution of 0.25°×0.3125° than in their study (2°×2.5°).

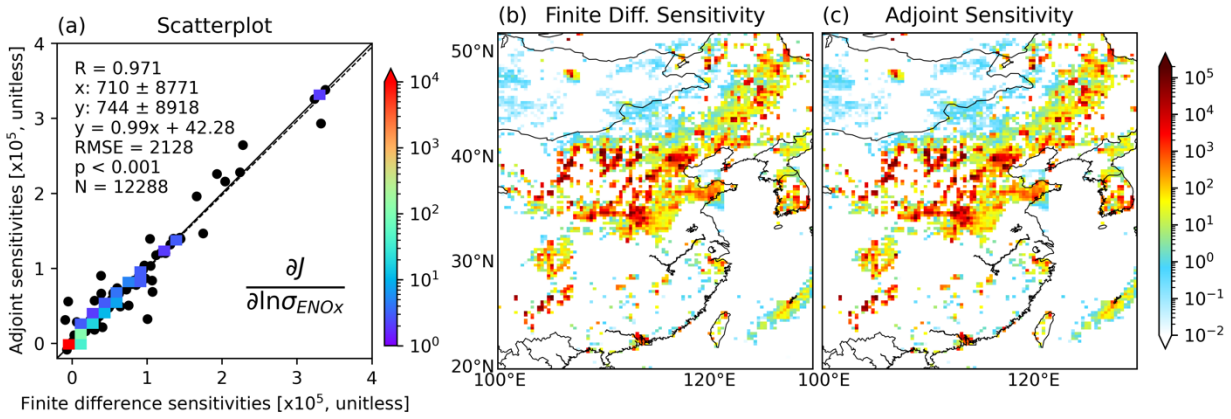

Figure C1. Comparison of adjoint sensitivities and finite difference sensitivities. (a) Scatter plot of the adjoint sensitivity of the cost function with respect to the logarithm of NOx emission scaling factor versus the finite difference sensitivities. The color scheme for panel (a) encodes the number of samples (the legend on the right of panel (a)). (b) Map of finite difference sensitivity. (c) Map of adjoint sensitivity.

Appendix D: Validation of HCHO simulations

It is not practical to validate the VOC emissions species by species in this study. We compare the GEOS-Chem simulation of HCHO with TROPOMI data for a rough validation of the VOC emissions. Overall, the GEOS-Chem simulations Baseline (2019) and 2020 Adjoint agree

well with TROPOMI HCHO in Feb.-Mar. of 2019 and 2020, respectively (Fig. D1). The correlation coefficients for the two comparisons are 0.878 and 0.874, and the MBE are -0.036 DU and -0.042 DU, respectively. This good agreement also supports our assumption of ignoring the change of VOC emissions from 2010 to 2019, since the anthropogenic VOC emission used for Baseline (2019) is equivalent to MIX 2010. However, Fig. D1 shows GEOS-Chem tends to overestimate the HCHO VCD over urban regions and underestimate it over rural regions, which indicates the partition of total emissions may overestimate the anthropogenic emissions and underestimate the biogenic emissions, at least for HCHO. A more comprehensive evaluation for various species and emission sectors would be helpful for further improvement of the VOC emissions used in the model.

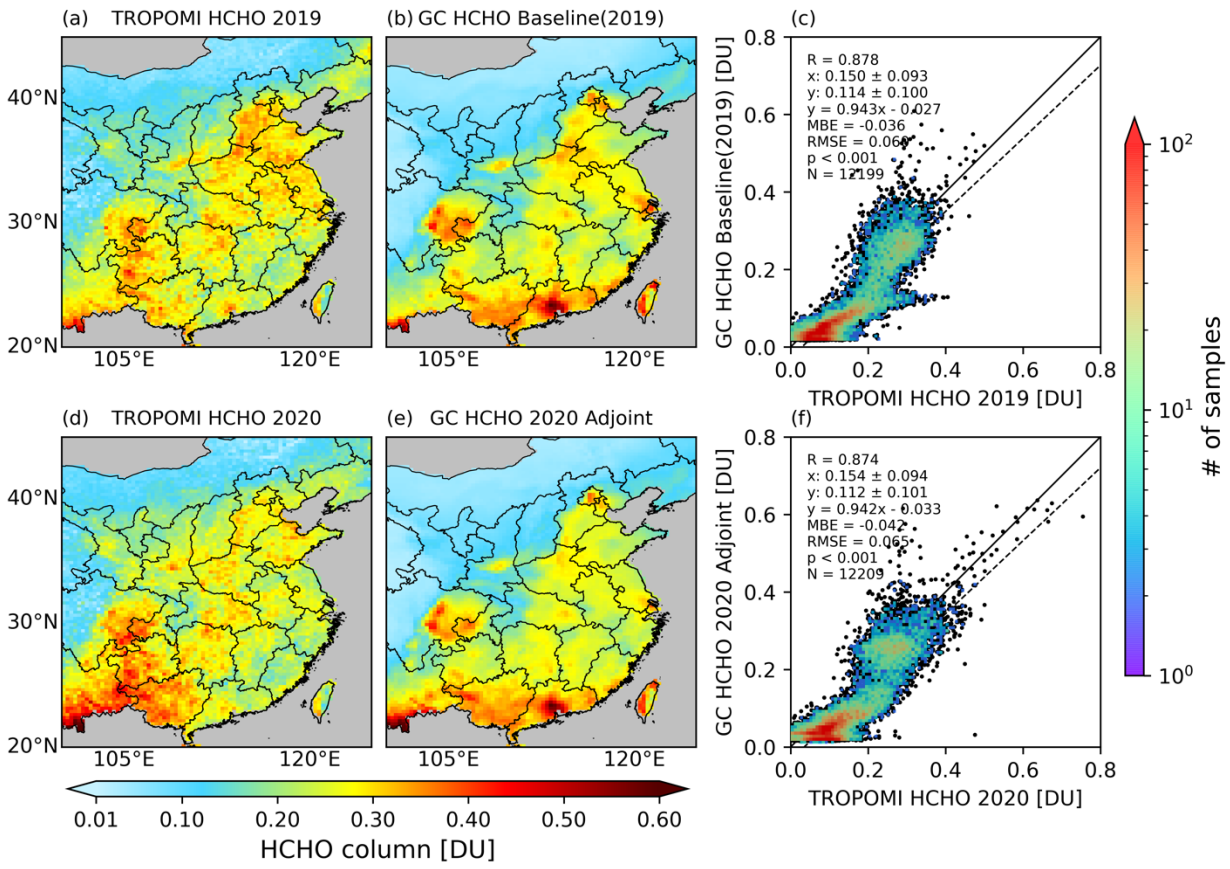

Figure D1. Comparison of tropospheric HCHO VCD from TROPOMI and GEOS-Chem. (a): TROPOMI HCHO in 2019 Feb.-Mar. (b): GEOS-Chem HCHO from Baseline (2019). (c): Scatter plot between (a) and (b). (d): TROPOMI HCHO in 2020 Feb. -Mar. (e): GEOS-Chem HCHO from

2020 Adjoint. (f): Scatter plot between (d) and (e). The emissions and meteorology configurations for GEOS-Chem simulations Baseline (2019) and 2020 Adjoint are listed in Table 1.

Data availability

The TROPOMI NO_2 and HCHO product are available at the NASA Goddard Earth Sciences Data and Information Services Center (https://daac.gsfc.nasa.gov). The ground O_3 and NO_2 measurements are available at the China National Environmental Monitoring Center (http://www.cnemc.cn/en/).

Author contribution

ZL and JW designed the research, and ZL conducted the research. YW, DKH and XC contributed to the research design. ZL and JW wrote the manuscript, and XC and DKH contributed to the writing. YW and TS developed the codes for comparing the tropospheric NO_2 VCD from model and TROPOMI data. KS developed the codes for oversampling.

Competing interests

The authors declare that they have no conflict of interest.

Acknowledgements

This research is supported by the NASA ACMAP program (grant number: 80NSSC19K0950). We acknowledge the computational support from the High-Performance Computing group at the University of Iowa.

References

Atkinson, R.: Atmospheric chemistry of VOCs and NOx, Atmospheric Environment, 34, 2063-2101, 10.1016/s1352-2310(99)00460-4, 2000.

742 Bauwens, M., Compernolle, S., Stavrakou, T., Muller, J. F., van Gent, J., Eskes, H., Levelt, P. F.,
743 van der A, R., Veefkind, J. P., Vlietinck, J., Yu, H., and Zehner, C.: Impact of Coronavirus
744 Outbreak on NO2 Pollution Assessed Using TROPOMI and OMI Observations, Geophys Res Lett,
745 47, 10.1029/2020GL087978, 2020.
746 Bey, I., Jacob, D. J., Yantosca, R. M., Logan, J. A., Field, B. D., Fiore, A. M., Li, Q., Liu, H. Y.,
747 Mickley, L. J., and Schultz, M. G.: Global modeling of tropospheric chemistry with assimilated
748 meteorology: Model description and evaluation, Journal of Geophysical Research: Atmospheres,
749 106, 23073-23095, 10.1029/2001jd000807, 2001.
750 Bi, Z., Ye, Z., He, C., and Li, Y.: Analysis of the meteorological factors affecting the short-term
751 increase in O3 concentrations in nine global cities during COVID-19, Atmospheric Pollution
752 Research, 13, 101523, https://doi.org/10.1016/j.apr.2022.101523, 2022.
753 Chen, D., Wang, Y., McElroy, M. B., He, K., Yantosca, R. M., and Le Sager, P.: Regional CO
754 pollution and export in China simulated by the high-resolution nested-grid GEOS-Chem model,
755 Atmospheric Chemistry and Physics, 9, 3825-3839, 10.5194/acp-9-3825-2009, 2009.
756 Cooper, M., Martin, R. V., Padmanabhan, A., and Henze, D. K.: Comparing mass balance and
757 adjoint methods for inverse modeling of nitrogen dioxide columns for global nitrogen oxide
758 emissions, Journal of Geophysical Research: Atmospheres, 122, 4718-4734,
759 10.1002/2016jd025985, 2017.
760 De Smedt, I., Theys, N., Yu, H., Danckaert, T., Lerot, C., Compernolle, S., Van Roozendael, M.,
761 Richter, A., Hilboll, A., Peters, E., Pedergnana, M., Loyola, D., Beirle, S., Wagner, T., Eskes, H.,
762 van Geffen, J., Boersma, K. F., and Veefkind, P.: Algorithm theoretical baseline for formaldehyde
763 retrievals from S5P TROPOMI and from the QA4ECV project, Atmospheric Measurement
764 Techniques, 11, 2395-2426, 10.5194/amt-11-2395-2018, 2018.
765 Eskes, H. J. and Boersma, K. F.: Averaging kernels for DOAS total-column satellite retrievals,
766 Atmospheric Chemistry and Physics, 3, 1285-1291, 10.5194/acp-3-1285-2003, 2003.
767 Ghahremanloo, M., Lops, Y., Choi, Y., and Mousavinezhad, S.: Impact of the COVID-19 outbreak
768 on air pollution levels in East Asia, Science of the Total Environment, 754,
769 10.1016/j.scitotenv.2020.142226, 2021.
770 Gong, C., Lei, Y., Ma, Y., Yue, X., and Liao, H.: Ozone–vegetation feedback through dry
771 deposition and isoprene emissions in a global chemistry–carbon–climate model, Atmos. Chem.
772 Phys., 20, 3841-3857, 10.5194/acp-20-3841-2020, 2020.

773 Guenther, A. B., Jiang, X., Heald, C. L., Sakulyanontvittaya, T., Duhl, T., Emmons, L. K., and
774 Wang, X.: The Model of Emissions of Gases and Aerosols from Nature version 2.1 (MEGAN2.1):
775 an extended and updated framework for modeling biogenic emissions, Geoscientific Model
776 Development, 5, 1471-1492, 10.5194/gmd-5-1471-2012, 2012.
777 Guo, J., Zhang, X. S., Gao, Y., Wang, Z. W., Zhang, M. G., Xue, W. B., Herrmann, H., Brasseur,
778 G. P., Wang, T., and Wang, Z.: Evolution of Ozone Pollution in China: What Track Will It Follow?,
779 Environmental Science & Technology, 57, 109-117, 10.1021/acs.est.2c08205, 2023.
780 Henze, D. K., Hakami, A., and Seinfeld, J. H.: Development of the adjoint of GEOS-Chem,
781 Atmospheric Chemistry and Physics, 7, 2413-2433, 10.5194/acp-7-2413-2007, 2007.
782 Henze, D. K., Seinfeld, J. H., and Shindell, D. T.: Inverse modeling and mapping US air quality
783 influences of inorganic PM2.5 precursor emissions using the adjoint of GEOS-Chem, Atmospheric
784 Chemistry and Physics, 9, 5877-5903, 10.5194/acp-9-5877-2009, 2009.
785 Hoesly, R. M., Smith, S. J., Feng, L., Klimont, Z., Janssens-Maenhout, G., Pitkanen, T., Seibert,
786 J. J., Vu, L., Andres, R. J., Bolt, R. M., Bond, T. C., Dawidowski, L., Kholod, N., Kurokawa, J.-
787 i., Li, M., Liu, L., Lu, Z., Moura, M. C. P., O'Rourke, P. R., and Zhang, Q.: Historical (1750–2014)
788 anthropogenic emissions of reactive gases and aerosols from the Community Emissions Data
789 System (CEDS), Geoscientific Model Development, 11, 369-408, 10.5194/gmd-11-369-2018,
790 2018.
791 Huang, X., Ding, A., Gao, J., Zheng, B., Zhou, D., Qi, X., Tang, R., Wang, J., Ren, C., Nie, W.,
792 Chi, X., Xu, Z., Chen, L., Li, Y., Che, F., Pang, N., Wang, H., Tong, D., Qin, W., Cheng, W., Liu,
793 W., Fu, Q., Liu, B., Chai, F., Davis, S. J., Zhang, Q., and He, K.: Enhanced secondary pollution
794 offset reduction of primary emissions during COVID-19 lockdown in China, National Science
795 Review, 8, 10.1093/nsr/nwaa137, 2020.
796 Hudman, R. C., Moore, N. E., Mebust, A. K., Martin, R. V., Russell, A. R., Valin, L. C., and
797 Cohen, R. C.: Steps towards a mechanistic model of global soil nitric oxide emissions:
798 implementation and space based-constraints, Atmospheric Chemistry and Physics, 12, 7779-7795,
799 10.5194/acp-12-7779-2012, 2012.
800 Janssens-Maenhout, G., Crippa, M., Guizzardi, D., Dentener, F., Muntean, M., Pouliot, G.,
801 Keating, T., Zhang, Q., Kurokawa, J., Wankmuller, R., van der Gon, H. D., Kuenen, J. J. P.,
802 Klimont, Z., Frost, G., Darras, S., Koffi, B., and Li, M.: HTAP_v2.2: a mosaic of regional and

803 global emission grid maps for 2008 and 2010 to study hemispheric transport of air pollution,
804 Atmospheric Chemistry and Physics, 15, 11411-11432, 10.5194/acp-15-11411-2015, 2015.
805 Jerrett, M., Burnett, R. T., Pope, C. A., Ito, K., Thurston, G., Krewski, D., Shi, Y. L., Calle, E.,
806 and Thun, M.: Long-Term Ozone Exposure and Mortality, New England Journal of Medicine, 360,
807 1085-1095, 10.1056/NEJMoa0803894, 2009.
808 Judd, L. M., Al-Saadi, J. A., Szykman, J. J., Valin, L. C., Janz, S. J., Kowalewski, M. G., Eskes,
809 H. J., Veefkind, J. P., Cede, A., Mueller, M., Gebetsberger, M., Swap, R., Pierce, R. B., Nowlan,
810 C. R., Abad, G. G., Nehrir, A., and Williams, D.: Evaluating Sentinel-5P TROPOMI tropospheric
811 NO2 column densities with airborne and Pandora spectrometers near New York City and Long
812 Island Sound, Atmospheric Measurement Techniques, 13, 6113-6140, 10.5194/amt-13-6113-2020,
813 2020.
814 Le, T. H., Wang, Y., Liu, L., Yang, J. N., Yung, Y. L., Li, G. H., and Seinfeld, J. H.: Unexpected
815 air pollution with marked emission reductions during the COVID-19 outbreak in China, Science,
816 369, 702-706, 10.1126/science.abb7431, 2020.
817 Leue, C., Wenig, M., Wagner, T., Klimm, O., Platt, U., and Jähne, B.: Quantitative analysis of
818 NOx emissions from Global Ozone Monitoring Experiment satellite image sequences, Journal of
819 Geophysical Research: Atmospheres, 106, 5493-5505, 10.1029/2000jd900572, 2001.
820 Levelt, P. F., Zweers, D. C. S., Aben, I., Bauwens, M., Borsdorff, T., De Smedt, I., Eskes, H. J.,
821 Lerot, C., Loyola, D. G., Romahn, F., Stavrakou, T., Theys, N., Van Roozendael, M., Veefkind, J.
822 P., and Verhoelst, T.: Air quality impacts of COVID-19 lockdown measures detected from space
823 using high spatial resolution observations of multiple trace gases from Sentinel-5P/TROPOMI,
824 Atmospheric Chemistry and Physics, 22, 10319-10351, 10.5194/acp-22-10319-2022, 2022.
825 Li, M., McDonald, B. C., McKeen, S. A., Eskes, H., Levelt, P., Francoeur, C., Harkins, C., He, J.,
826 Barth, M., Henze, D. K., Bela, M. M., Trainer, M., de Gouw, J. A., and Frost, G. J.: Assessment
827 of Updated Fuel-Based Emissions Inventories Over the Contiguous United States Using
828 TROPOMI NO2 Retrievals, Journal of Geophysical Research-Atmospheres, 126,
829 10.1029/2021jd035484, 2021.
830 Li, M., Zhang, Q., Kurokawa, J.-i., Woo, J.-H., He, K., Lu, Z., Ohara, T., Song, Y., Streets, D. G.,
831 Carmichael, G. R., Cheng, Y., Hong, C., Huo, H., Jiang, X., Kang, S., Liu, F., Su, H., and Zheng,
832 B.: MIX: a mosaic Asian anthropogenic emission inventory under the international collaboration

framework of the MICS-Asia and HTAP, Atmospheric Chemistry and Physics, 17, 935-963, 10.5194/acp-17-935-2017, 2017.

Liu, F., Page, A., Strode, S. A., Yoshida, Y., Choi, S., Zheng, B., Lamsal, L. N., Li, C., Krotkov, N. A., Eskes, H., van der A, R., Veefkind, P., Levelt, P. F., Hauser, O. P., and Joiner, J.: Abrupt decline in tropospheric nitrogen dioxide over China after the outbreak of COVID-19, Science Advances, 6, 10.1126/sciadv.abc2992, 2020a.

Liu, S. C., Trainer, M., Fehsenfeld, F. C., Parrish, D. D., Williams, E. J., Fahey, D. W., Hubler, G., and Murphy, P. C.: Ozone production in the rural troposphere and the implications for regional and global ozone distributions, Journal of Geophysical Research-Atmospheres, 92, 4191-4207, 10.1029/JD092iD04p04191, 1987.

Liu, T., Wang, X., Hu, J., Wang, Q., An, J., Gong, K., Sun, J., Li, L., Qin, M., Li, J., Tian, J., Huang, Y., Liao, H., Zhou, M., Hu, Q., Yan, R., Wang, H., and Huang, C.: Driving Forces of Changes in Air Quality during the COVID-19 Lockdown Period in the Yangtze River Delta Region, China, Environmental Science & Technology Letters, 7, 779-786, 10.1021/acs.estlett.0c00511, 2020b.

Liu, Y. M., Wang, T., Stavrakou, T., Elguindi, N., Doumbia, T., Granier, C., Bouarar, I., Gaubert, B., and Brasseur, G. P.: Diverse response of surface ozone to COVID-19 lockdown in China, Science of the Total Environment, 789, 10.1016/j.scitotenv.2021.147739, 2021.

Lu, X., Zhang, L., Chen, Y. F., Zhou, M., Zheng, B., Li, K., Liu, Y. M., Lin, J. T., Fu, T. M., and Zhang, Q.: Exploring 2016-2017 surface ozone pollution over China: source contributions and meteorological influences, Atmospheric Chemistry and Physics, 19, 8339-8361, 10.5194/acp-19-8339-2019, 2019.

Mao, J., Paulot, F., Jacob, D. J., Cohen, R. C., Crounse, J. D., Wennberg, P. O., Keller, C. A., Hudman, R. C., Barkley, M. P., and Horowitz, L. W.: Ozone and organic nitrates over the eastern United States: Sensitivity to isoprene chemistry, Journal of Geophysical Research: Atmospheres, 118, 11,256-211,268, 10.1002/jgrd.50817, 2013.

Mao, J., Jacob, D. J., Evans, M. J., Olson, J. R., Ren, X., Brune, W. H., Clair, J. M. S., Crounse, J. D., Spencer, K. M., Beaver, M. R., Wennberg, P. O., Cubison, M. J., Jimenez, J. L., Fried, A., Weibring, P., Walega, J. G., Hall, S. R., Weinheimer, A. J., Cohen, R. C., Chen, G., Crawford, J. H., McNaughton, C., Clarke, A. D., Jaeglé, L., Fisher, J. A., Yantosca, R. M., Le Sager, P., and

863 Carouge, C.: Chemistry of hydrogen oxide radicals (HOx) in the Arctic troposphere in spring,
864 Atmospheric Chemistry and Physics, 10, 5823-5838, 10.5194/acp-10-5823-2010, 2010.
865 Martin, R. V., Jacob, D. J., Chance, K., Kurosu, T. P., Palmer, P. I., and Evans, M. J.: Global
866 inventory of nitrogen oxide emissions constrained by space-based observations of NO2 columns,
867 Journal of Geophysical Research-Atmospheres, 108, 10.1029/2003jd003453, 2003.
868 Miyazaki, K., Bowman, K., Sekiya, T., Jiang, Z., Chen, X., Eskes, H., Ru, M., Zhang, Y., and
869 Shindell, D.: Air Quality Response in China Linked to the 2019 Novel Coronavirus (COVID-19)
870 Lockdown, Geophys Res Lett, 47, 10.1029/2020gl089252, 2020.
871 Murray, L. T., Jacob, D. J., Logan, J. A., Hudman, R. C., and Koshak, W. J.: Optimized regional
872 and interannual variability of lightning in a global chemical transport model constrained by
873 LIS/OTD satellite data, Journal of Geophysical Research: Atmospheres, 117,
874 10.1029/2012jd017934, 2012.
875 Ott, L. E., Pickering, K. E., Stenchikov, G. L., Allen, D. J., DeCaria, A. J., Ridley, B., Lin, R.-F.,
876 Lang, S., and Tao, W.-K.: Production of lightning NOx and its vertical distribution calculated from
877 three-dimensional cloud-scale chemical transport model simulations, Journal of Geophysical
878 Research, 115, 10.1029/2009jd011880, 2010.
879 Palmer, P. I., Jacob, D. J., Chance, K., Martin, R. V., Spurr, R. J. D., Kurosu, T. P., Bey, I.,
880 Yantosca, R., Fiore, A., and Li, Q. B.: Air mass factor formulation for spectroscopic measurements
881 from satellites: Application to formaldehyde retrievals from the Global Ozone Monitoring
882 Experiment, Journal of Geophysical Research-Atmospheres, 106, 14539-14550,
883 10.1029/2000jd900772, 2001.
884 Pusede, S. E., Steiner, A. L., and Cohen, R. C.: Temperature and Recent Trends in the Chemistry
885 of Continental Surface Ozone, Chemical Reviews, 115, 3898-3918, 10.1021/cr5006815, 2015.
886 Qu, Z., Henze, D. K., Capps, S. L., Wang, Y., Xu, X., Wang, J., and Keller, M.: Monthly top-down
887 NOx emissions for China (2005–2012): A hybrid inversion method and trend analysis, Journal of
888 Geophysical Research: Atmospheres, 122, 4600-4625, https://doi.org/10.1002/2016JD025852,
889 2017.
890 Qu, Z., Henze, D. K., Li, C., Theys, N., Wang, Y., Wang, J., Wang, W., Han, J., Shim, C.,
891 Dickerson, R. R., and Ren, X.: SO2 Emission Estimates Using OMI SO2 Retrievals for 2005-2017,
892 J Geophys Res Atmos, 124, 8336-8359, 10.1029/2019JD030243, 2019.

Sha, T., Ma, X. Y., Zhang, H. X., Janechek, N., Wang, Y. Y., Wang, Y., Garcia, L. C., Jenerette, G. D., and Wang, J.: Impacts of Soil NOx Emission on O-3 Air Quality in Rural California, Environmental Science & Technology, 55, 7113-7122, 10.1021/acs.est.0c06834, 2021.

Shi, X. and Brasseur, G. P.: The Response in Air Quality to the Reduction of Chinese Economic Activities During the COVID-19 Outbreak, Geophys Res Lett, 47, 10.1029/2020gl088070, 2020.

Sillman, S., Logan, J. A., and Wofsy, S. C.: The sensitivity of ozone to nitrogen-oxides and hydrocarbons in regional ozone episodes, Journal of Geophysical Research-Atmospheres, 95, 1837-1851, 10.1029/JD095iD02p01837, 1990.

Steinbacher, M., Zellweger, C., Schwarzenbach, B., Bugmann, S., Buchmann, B., Ordóñez, C., Prevot, A. S. H., and Hueglin, C.: Nitrogen oxide measurements at rural sites in Switzerland: Bias of conventional measurement techniques, Journal of Geophysical Research: Atmospheres, 112, https://doi.org/10.1029/2006JD007971, 2007.

Streets, D. G., Canty, T., Carmichael, G. R., de Foy, B., Dickerson, R. R., Duncan, B. N., Edwards, D. P., Haynes, J. A., Henze, D. K., Houyoux, M. R., Jacob, D. J., Krotkov, N. A., Lamsal, L. N., Liu, Y., Lu, Z., Martin, R. V., Pfister, G. G., Pinder, R. W., Salawitch, R. J., and Wecht, K. J.: Emissions estimation from satellite retrievals: A review of current capability, Atmospheric Environment, 77, 1011-1042, 10.1016/j.atmosenv.2013.05.051, 2013.

Sun, K., Zhu, L., Cady-Pereira, K., Chan Miller, C., Chance, K., Clarisse, L., Coheur, P.-F., González Abad, G., Huang, G., Liu, X., Van Damme, M., Yang, K., and Zondlo, M.: A physics-based approach to oversample multi-satellite, multispecies observations to a common grid, Atmospheric Measurement Techniques, 11, 6679-6701, 10.5194/amt-11-6679-2018, 2018.

Tong, L., Liu, Y., Meng, Y., Dai, X. R., Huang, L. J., Luo, W. X., Yang, M. R., Pan, Y., Zheng, J., and Xiao, H.: Surface ozone changes during the COVID-19 outbreak in China: An insight into the pollution characteristics and formation regimes of ozone in the cold season, Journal of Atmospheric Chemistry, 80, 103-120, 10.1007/s10874-022-09443-2, 2023.

Travis, K. R., Jacob, D. J., Keller, C. A., Kuang, S., Lin, J., Newchurch, M. J., and Thompson, A. M.: Resolving ozone vertical gradients in air quality models, Atmos. Chem. Phys. Discuss., 2017, 1-18, 10.5194/acp-2017-596, 2017.

Travis, K. R., Jacob, D. J., Fisher, J. A., Kim, P. S., Marais, E. A., Zhu, L., Yu, K., Miller, C. C., Yantosca, R. M., Sulprizio, M. P., Thompson, A. M., Wennberg, P. O., Crounse, J. D., St Clair, J. M., Cohen, R. C., Laughner, J. L., Dibb, J. E., Hall, S. R., Ullmann, K., Wolfe, G. M., Pollack, I.

924 B., Peischl, J., Neuman, J. A., and Zhou, X.: Why do Models Overestimate Surface Ozone in the
925 Southeastern United States?, Atmos Chem Phys, 16, 13561-13577, 10.5194/acp-16-13561-2016,
926 2016.
927 van der Werf, G. R., Randerson, J. T., Giglio, L., van Leeuwen, T. T., Chen, Y., Rogers, B. M.,
928 Mu, M., van Marle, M. J. E., Morton, D. C., Collatz, G. J., Yokelson, R. J., and Kasibhatla, P. S.:
929 Global fire emissions estimates during 1997–2016, Earth System Science Data, 9, 697-720,
930 10.5194/essd-9-697-2017, 2017.
931 TROPOMI ATBD of the total and tropospheric NO2 data products:
932 https://sentinel.esa.int/documents/247904/2476257/sentinel-5p-tropomi-atbd-no2-data-products,
933 last access: Sep. 29.
934 van Geffen, J., Boersma, K. F., Eskes, H., Sneep, M., ter Linden, M., Zara, M., and Veefkind, J.
935 P.: S5P TROPOMI NO2 slant column retrieval: method, stability, uncertainties and comparisons
936 with OMI, Atmospheric Measurement Techniques, 13, 1315-1335, 10.5194/amt-13-1315-2020,
937 2020.
938 Veefkind, J. P., Aben, I., McMullan, K., Förster, H., de Vries, J., Otter, G., Claas, J., Eskes, H. J.,
939 de Haan, J. F., Kleipool, Q., van Weele, M., Hasekamp, O., Hoogeveen, R., Landgraf, J., Snel, R.,
940 Tol, P., Ingmann, P., Voors, R., Kruizinga, B., Vink, R., Visser, H., and Levelt, P. F.: TROPOMI
941 on the ESA Sentinel-5 Precursor: A GMES mission for global observations of the atmospheric
942 composition for climate, air quality and ozone layer applications, Remote Sensing of Environment,
943 120, 70-83, https://doi.org/10.1016/j.rse.2011.09.027, 2012.
944 Venter, Z. S., Aunan, K., Chowdhury, S., and Lelieveld, J.: COVID-19 lockdowns cause global
945 air pollution declines, Proceedings of the National Academy of Sciences, 117, 18984-18990,
946 doi:10.1073/pnas.2006853117, 2020.
947 Verhoelst, T., Compernolle, S., Pinardi, G., Lambert, J. C., Eskes, H. J., Eichmann, K. U., Fjæraa,
948 A. M., Granville, J., Niemeijer, S., Cede, A., Tiefengraber, M., Hendrick, F., Pazmiño, A., Bais,
949 A., Bazureau, A., Boersma, K. F., Bognar, K., Dehn, A., Donner, S., Elokhov, A., Gebetsberger,
950 M., Goutail, F., de la Mora, M. G., Gruzdev, A., Gratsea, M., Hansen, G. H., Irie, H., Jepsen, N.,
951 Kanaya, Y., Karagkiozidis, D., Kivi, R., Kreher, K., Levelt, P. F., Liu, C., Müller, M., Comas, M.
952 N., Piters, A. J. M., Pommereau, J. P., Portafaix, T., Prados-Roman, C., Puentedura, O., Querel,
953 R., Remmers, J., Richter, A., Rimmer, J., Cárdenas, C. R., de Miguel, L. S., Sinyakov, V. P.,
954 Stremme, W., Strong, K., Van Roozendael, M., Veefkind, J. P., Wagner, T., Wittrock, F., González,

M. Y., and Zehner, C.: Ground-based validation of the Copernicus Sentinel-5P TROPOMI NO2 measurements with the NDACC ZSL-DOAS, MAX-DOAS and Pandonia global networks, Atmospheric Measurement Techniques, 14, 481-510, 10.5194/amt-14-481-2021, 2021.

Vigouroux, C., Langerock, B., Aquino, C. A. B., Blumenstock, T., Cheng, Z. B., De Mazière, M., De Smedt, I., Grutter, M., Hannigan, J. W., Jones, N., Kivi, R., Loyola, D., Lutsch, E., Mahieu, E., Makarova, M., Metzger, J. M., Morino, I., Murata, I., Nagahama, T., Notholt, J., Ortega, I., Palm, M., Pinardi, G., Röhling, A., Smale, D., Stremme, W., Strong, K., Sussmann, R., Té, Y., van Roozendael, M., Wang, P. C., and Winkler, H.: TROPOMI-Sentinel-5 Precursor formaldehyde validation using an extensive network of ground-based Fourier-transform infrared stations, Atmospheric Measurement Techniques, 13, 3751-3767, 10.5194/amt-13-3751-2020, 2020.

Vinken, G. C. M., Boersma, K. F., van Donkelaar, A., and Zhang, L.: Constraints on ship NOx emissions in Europe using GEOS-Chem and OMI satellite NO2 observations, Atmos. Chem. Phys., 14, 1353-1369, 10.5194/acp-14-1353-2014, 2014.

Wang, Y., Wang, J., Xu, X., Henze, D. K., Qu, Z., and Yang, K.: Inverse modeling of SO_2 and NO_x emissions over China using multisensor satellite data – Part 1: Formulation and sensitivity analysis, Atmospheric Chemistry and Physics, 20, 6631-6650, 10.5194/acp-20-6631-2020, 2020a.

Wang, Y., Wang, J., Zhou, M., Henze, D. K., Ge, C., and Wang, W.: Inverse modeling of SO_2 and NO_x emissions over China using multisensor satellite data – Part 2: Downscaling techniques for air quality analysis and forecasts, Atmospheric Chemistry and Physics, 20, 6651-6670, 10.5194/acp-20-6651-2020, 2020b.

Wang, Y. X., McElroy, M. B., Jacob, D. J., and Yantosca, R. M.: A nested grid formulation for chemical transport over Asia: Applications to CO, Journal of Geophysical Research: Atmospheres, 109, n/a-n/a, 10.1029/2004jd005237, 2004.

Williams, J. and Koppmann, R.: Volatile Organic Compounds in the Atmosphere: An Overview, in: Volatile Organic Compounds in the Atmosphere, 1-32, https://doi.org/10.1002/9780470988657.ch1, 2007.

Zhang, L., Jacob, D. J., Knipping, E. M., Kumar, N., Munger, J. W., Carouge, C. C., van Donkelaar, A., Wang, Y. X., and Chen, D.: Nitrogen deposition to the United States: distribution, sources, and processes, Atmospheric Chemistry and Physics, 12, 4539-4554, 10.5194/acp-12-4539-2012, 2012.

Zhang, Q., Pan, Y., He, Y., Walters, W. W., Ni, Q., Liu, X., Xu, G., Shao, J., and Jiang, C.: Substantial nitrogen oxides emission reduction from China due to COVID-19 and its impact on

surface ozone and aerosol pollution, Science of The Total Environment, 753, 10.1016/j.scitotenv.2020.142238, 2021.

Zhang, R. X., Zhang, Y. Z., Lin, H. P., Feng, X., Fu, T. M., and Wang, Y. H.: NOx Emission Reduction and Recovery during COVID-19 in East China, Atmosphere, 11, 10.3390/atmos11040433, 2020.

Zhang, Y.-L. and Cao, F.: Fine particulate matter (PM2.5) in China at a city level, Scientific Reports, 5, 14884, 10.1038/srep14884, 2015.

Zhao, Y., Zhang, K., Xu, X., Shen, H., Zhu, X., Zhang, Y., Hu, Y., and Shen, G.: Substantial Changes in Nitrogen Dioxide and Ozone after Excluding Meteorological Impacts during the COVID-19 Outbreak in Mainland China, Environmental Science & Technology Letters, 7, 402-408, 10.1021/acs.estlett.0c00304, 2020.

Zheng, B., Tong, D., Li, M., Liu, F., Hong, C., Geng, G., Li, H., Li, X., Peng, L., Qi, J., Yan, L., Zhang, Y., Zhao, H., Zheng, Y., He, K., and Zhang, Q.: Trends in China's anthropogenic emissions since 2010 as the consequence of clean air actions, Atmospheric Chemistry and Physics, 18, 14095-14111, 10.5194/acp-18-14095-2018, 2018.